IEEE Access
Multidisciplinary | Rapid Review | Open Access Journal

Received 1 March 2024, accepted 30 March 2024, date of publication 10 April 2024, date of current version 30 April 2024.

*Digital Object Identifier 10.1109/ACCESS.2024.3386920*

RESEARCH ARTICLE

# Validation of Passivity-Based Control and Array PID in High-Power Quadratic Buck Converter Through Rapid Prototyping

**RAFAEL ANTONIO ACOSTA-RODRÍGUEZ[1], (Member, IEEE), FREDY HERNÁN MARTINEZ-SARMIENTO[2], (Member, IEEE), GERMAN ARDUL MÚÑOZ-HERNANDEZ[3], (Senior Member, IEEE), EDGAR ALFREDO PORTILLA-FLORES[4], (Member, IEEE), AND OCTAVIO JOSÉ SALCEDO-PARRA[5], (Member, IEEE)**

[1]Smart Internet Research Group, Armos Group Colciencias, Distrital University Francisco José de Caldas, Bogotá 111611, Colombia
[2]Armos Group Colciencias, Universidad Distrital Francisco José de Caldas, Bogotá 111611, Colombia
[3]Department of Electronic Sciences, Meritorious Autonomous University of Puebla (BUAP), Puebla 72592, Mexico
[4]Unidad Profesional Interdisciplinaria de Ingeniería, Campus Tlaxcala, Instituto Politécnico Nacional (IPN), Tlaxcala 07738, Mexico
[5]Smart Internet Research Group Colciencias, Universidad Distrital Francisco José de Caldas, Bogotá 111611, Colombia

Corresponding author: Rafael Antonio Acosta-Rodríguez (raacostar@udistrital.edu.co)

This work was supported in part by the Armos Group and the Smart Internet Research Group, Universidad Distrital Francisco José de Caldas, Bogotá, Colombia; in part by the Ph.D. Internship at the Instituto Politecnico Nacional (IPN), Mexico City, in 2021, through the DISRYM Program; in part by the Ph.D. Program in Robotic and Mechatronic Systems Engineering; and in part by the Research Faculty, Facilities, and Laboratories at the Autonomous University of Puebla (BUAP), Mexico.

**ABSTRACT** This manuscript describes a swift control prototyping (SCP) approach implemented within an industrial setting, utilizing a DC-DC nonlinear quadratic buck converter (QBC) to decrease production expenses of electronic materials and devices while improving power system efficiency. A practical experimental setup is utilized to develop a working prototype, transforming 380 VDC to 48 VDC with a power capacity of up to 500 W. The setup incorporates dSPACE CP1103 to execute Model in the Loop (MIL), Software in the Loop (SIL), and Hardware in the Loop (HIL) methodologies. Additionally, it employs advanced control strategies such as passivity-based control (PCB) and canonical forms, which are compared with classical Proportional-Integral-Derivative (PID) control arrangements to propose a comprehensive control scheme that ensures stability in the presence of real-time disturbances (RT). Finally, a performance analysis is conducted, assessing important indicators like reaction time, precision of signals, stability of the system, and efficiency in resource utilization. The document concludes by offering a performance evaluation that encompasses PI, Cp, CpK, Z-score, and ITAE. This assessment considers factors such as response time, signal accuracy, system stability, and the efficiency of resource utilization.

**INDEX TERMS** Canonic forms, dSPACE, hardware in the loop (HIL), model in the loop (MIL), passivity-based control (PBC), performance indices, proportional-integral-derivative (PID) array, quadratic buck converter (QBC), rapid control prototyping (RCP), real-time (RT), software in the loop (SIL).

## I. INTRODUCTION

### A. MOTIVATION AND INCITEMENT

Recent progress in the engineering and optimization of DC converters has led to the introduction of critical innovations. These include versatile operational modes, DC interfaces, elevated gain ratios for voltage, the ability to convert power in both directions, and improved operational efficiency [1], [2], [3], [4]. Such advancements hold significant promise for transforming the landscape of energy conversion techniques, offering valuable benefits for multiple industries such as renewable energy sources,

The associate editor coordinating the review of this manuscript and approving it for publication was Lei Chen.

systems for storing energy, and the field of power electronics [1], [2], [3], [4].

The domain of power conversion has witnessed the evolution of various strategies and configurations for converting direct current (DC) to direct current (DC), aiming to enhance efficiency and versatility for a broad range of uses. Within this realm, the development of transformer less converters stands out, offering notable benefits by reducing size, weight, and expense. A critical advancement in this area is the creation of a transformer less DC/DC converter that operates in dual modes and features a continuous input current port, marking a substantial advancement in the field [1]. Furthermore, the innovation of a transformer-less quadratic buck-boost converter that achieves a high voltage gain ratio and maintains continuous current flow at both input and output ports has been introduced, showcasing significant enhancements in efficiency and functionality over conventional converter designs [2].

In the area of direct current (DC) to alternating current (AC) conversion technology, the introduction of a four-quadrant buck converter featuring a unified ground has facilitated the ability to convert power bidirectionally between DC and AC forms. This innovation is especially relevant in the context of renewable energy systems and energy storage solutions. Moreover, the unveiling of a non-isolated DC-DC converter that operates in two distinct modes and delivers a positive voltage output marks a significant improvement in the adaptability and performance of power conversion for targeted uses [3], [4].

Conventional methodologies for the design and production of converters usually require comprehensive empirical testing, precise measurements, and detailed experimental validation of every element within a quadratic converter [5]. As a result, scaling up to large-scale production is rendered a more intricate and protracted process [6].

In contrast, the investigation and confirmation of contemporary control strategies within quadratic converters, known for their nonlinear dynamics, require a series of steps that do not follow an established methodical linkage, encompassing procedures that are laborious and time intensive. This complexity frequently hinders the practical application of such techniques via empirical experimentation in various contexts [7].

The utilization of fast prototyping techniques presents a pivotal chance to refine industrial operations significantly. By employing computer-generated simulations, these methodologies enable a decrease in surplus costs related to time, components, and materials. Consequently, there is an enhancement in the productivity of production and the instantaneous adaptability of the deployed control systems to disruptions. This approach provides extensive options for conversion and energy use, facilitated by the Software in the Loop (SIL) instrument [8].

Employing dSPACE for rapid prototyping involves utilizing hardware-in-the-loop (HIL) systems branded by dSPACE for the preliminary creation and assessment of electronic and control mechanisms in diverse sectors, such as the automotive and aerospace industries [8].

dSPACE stands out as a premier source of simulation and testing resources aimed at enhancing electronic and control systems. The company's hardware-in-the-loop (HIL) systems facilitate the real-time simulation of electronic component actions, simplifying the process of system assessment in a virtual setting before actual deployment [8].

Rapid prototyping utilizing dSPACE enables the development of virtual models for intricate systems, including vehicle management systems, propulsion mechanisms, or avionics. These virtual models provide engineers the capability to enhance and confirm control algorithms, execute detailed functional examinations, and evaluate the efficacy of systems in a safe and regulated setting [8].

Utilizing dSPACE for quick prototyping accelerates the development timeline, diminishes expenses, and lowers the hazards linked to the actual deployment of systems. Furthermore, dSPACE offers an extensive array of tools and templates for design and simulation, which streamline the creation of sophisticated and precise virtual prototypes [8].

The rapid prototyping approach aids in determining the ideal device parameters for designing quadratic converter configurations, with an emphasis on aspects like efficiency, availability, performance, and economic viability. Additionally, it supports the accurate tuning of variables that control operating states and balance conditions when facing disruptions throughout the enactment of the suggested control mechanism [7], [8].

### B. LITERATURE REVIEW

Recent developments in DC converter design underscore the importance of parameterization adjustments in nonlinear models [7]. These adjustments simplify the creation of standardized assemblies, leading to cost savings in implementation, manufacturing, and extensive laboratory testing.

To establish precise control implementation dynamics, various acquisition cards like FPGA, Arduino, Raspberry Pi4, DSP, or dSPACE are employed, configuring PWM (Pulse Width Modulation) tailored to the plant's physical requirements [8]. Digitally treating signals through discretization in line with the plant facilitates real-time (RT) control and monitoring, mitigating device saturation and overheating issues that can lead to energy losses or system malfunction.

The control strategy starts with the initial mathematical model design, which necessitates linearization despite presenting a dynamic system of the fourth order with right-sided zeros presents difficulties when implementing a single control loop [10].

Buck converters with switched power play a vital function in producing voltage and current within electronic circuits, ensuring reliable power supply from a primary source [11], [12]. DC-DC converters, in turn, adapt signals to desired continuous values [13].

Simulation in the loop (SIL) stands out as a methodology that allows both controller and plant simulation on the same simulator without input or output utilization, preserving signal integrity. SIL offers advantages over RCP and HIL by ensuring signal integrity and enabling running both the controller and plant models on a single simulator is a requirement [14].

Buck converters typically sit between a primary power source and a load, usually electrical, providing a direct voltage supply to power various digital electronic devices. The control loop of the system adjusts the conduction time of the commutator element, improving response time and stability in the face of disturbances [6], [11], [13], [15].

The system demonstrates non-linear characteristics because of its variable structure, necessitating the use and confirmation of non-linear control methods such as Passivity-Based Control (PBC) and PID control techniques when dealing with time-varying disturbances [16].

The suggested method, utilizing Rapid Control Prototyping (RCP) and the Software in the Loop (SIL) technique, integrates the complete program into the target environment. This enables monitoring via Model in the Loop (MIL) and embedded development within an acquisition card or microprocessor, thus optimizing the plant's design, control models, and dynamic configuration for different operating points in real-time (RTS) [14].

The focus of this project is on creating an electronic nonlinear system specifically designed for managing commutated DC converters. It highlights the application of nonlinear control methods throughout the entire process, from modeling to execution, with potential uses in enhancing different industrial electrical operations. By optimizing these processes, the project aims to reduce energy consumption, increase safety measures, shorten implementation schedules, enhance response rates, and ensure efficient electrical transfer control [14].

The assessment of control system performance optimization utilizes the Integral Time of Absolute Error (ITAE) index. ITAE's distinctive sensitivity to large errors and robustness to noise makes it a suitable choice for assessing control stability, accuracy, and response time in noisy conditions [17], [18], [19], [20].

ITAE offers the flexibility to optimize controller parameters by minimizing the index. Its independence from the system's operating point allows for performance comparison across different points of operation. Furthermore, its robustness against noise ensures that control performance can be assessed in noisy environments, particularly relevant in switching converter control applications [20].

### C. CONTRIBUTION AND PAPER ORGANIZATION

This manuscript is structured as follows:

Section II elaborates on the construction of comprehensive mathematical models for the dynamic QBC system, presenting its portrayal through variables and state equations.

In section III the switched model is developed, which has the purpose of knowing the changes in the behavior of the system, in its different states, the variable ''u'' represents the input or control signal that is used to modify the behavior of a system. and achieve a desired response.

In Section IV, attention is given to the average model, which elucidates the dynamic characteristics of the periodic system. In this instance, it is applied to scrutinize the system's behavior under steady-state conditions.

Section V determines the linearization of the system as a tool to design automatic control systems that can control complex systems in RT, in this case from the transfer function of the plant.

Within Section VI, the static design phase encompasses the formulation of all construction equations pertinent to the quadratic Buck converter. Factors like the duty cycle are considered to establish accurate device parameters for constructing the system. Evaluation of outputs and their effectiveness is carried out as a component of this procedure.

Section VII integrates passivity-based control, aimed at ensuring that the output voltage of the converter adheres to a specified reference while minimizing the energy stored within the converter, which in turn reduces the effects of voltage fluctuation. load and disturbances on the system, error dynamics passive output feedback error accurate where error dynamics refers to how the system's response to an input or disturbance affects system error, accuracy is the ability of the control system to keep the output error as low as possible, despite disturbances and fluctuations in operational circumstances, the obtained results are thoroughly examined.

Section VIII, the canonical forms applied to the QBC are used, as a tool to design passive systems, with which it is possible to analyze and design linear dynamic systems in a systematic and standardized way, as well as create a controller design, it is implemented. the control loop for passive canonical forms as a control technique that uses the canonical forms of interconnection or energy dissipation to design passive control systems that converge to a desired reference signal.

In section IX, the third classic PID control for the converter is developed, which incorporates an arrangement using an S function algorithm to optimize the response in values of shorter times.

In section X the experimental development is presented, which contains two parts,the first phase involves creating the PCB (Printed Circuit Board) and assembling the corresponding QBC (Quadratic Buck Converter) or system plant. The second phase consists of rapidly prototyping the design using the dSPACE 1103, where the passivity and the PID array within the converter undergo validation through simulated testing using Control Desk, a tool utilized for the development and setup of real-time control systems. This validation is conducted before experimental testing, comparing the simulated results with the actual electrical response observed on the oscilloscope, as previously described (Acosta-Rodríguez, 2023) [43].

This document provides a comprehensive investigation of the dynamic Quadratic Buck Converter (QBC) system. It covers various aspects, including mathematical modeling, the creation of control strategies of passivity-based control (PCB) and canonical forms, which are compared with classical Proportional-Integral-Derivative (PID) control arrangements, and rigorous experimental validation. The main objective is to improve the stability of the system, reduce energy storage requirements, and achieve precise control, even when dealing with disturbances and changing operating conditions.

In Section XI we analyze the results, presenting the methodological process used for the analysis, the results that are analyzed according to the type of index reveal a strong performance of the control, where PI (Absolute Error Time Integral): All control values very close to zero in several variables. For example, in vC1, the Passivity-Based Control (PBC) has a value of '1.04e-03' and the PID array has '2.49e-9'. In iL1, PBC is '1.56e-02', whereas the PID array is '2.05e-00'. In iL2, you have PBC with '0.001468795' and the PID matrix is '1.37'. For Vc2, PBC is '7.35e-04' and its PID matrix is '6.12e-02'.

Under CPU (Process Capacity): CPU values are close to 1, suggesting that the process has sufficient capacity. However, the highest values in the PID matrix stand out, especially for iL1 is '2.4300400981' and iL2 is '10.4243232'.

Z-score: The values for the Z-score are relatively low in PBC, indicating a good fit with expectations. For example, in vC1 it is '0.52891368', in iL1 it is '0.04123456' and in iL2 it is '0.00120805'. and for the PID matrix, the values are very small.

The results underscore the stability and efficiency of control strategies, providing useful insights for real-world implementations. Key conclusions outlined in Section XII offer additional understanding regarding the efficacy of these control strategies and their potential real-world applications.

## II. MODEL OF QUADRATIC BUCK SWITCHED CONVERTER

The circuits QBC, generated through MATLAB software, depict the ON and OFF phases as shown in Figure 1, also referencing figures 1 and 2 from the previous paper [43].

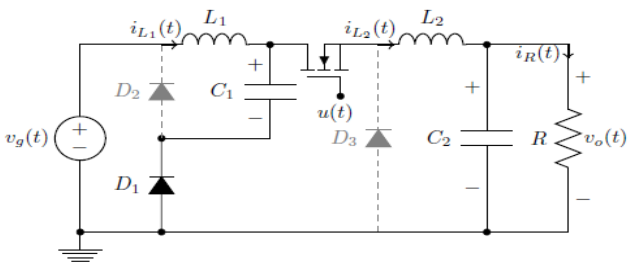


**FIGURE 1.** Active state of quadratic buck.

Below, we outline the equations that characterize the quadratic Buck circuits (QBC).

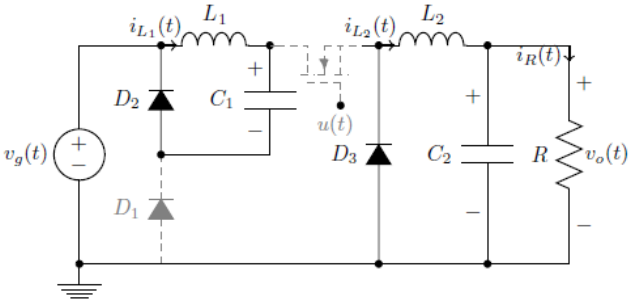


**FIGURE 2.** Quadratic buck in the OFF state.

### A. REPRESENTATION OF THE EQUATIONS IN STATE ON

The ON state behavior, as depicted in Figure 1, yields the following equations:

$$V_g = V_{L1} + V_{C1} \tag{1}$$
$$V_{C1} = V_{L2} + V_{C2} \tag{2}$$
$$I_{L1} = V_{C1} + I_{L2} \tag{3}$$
$$I_{L2} = I_{C2} + I_R \tag{4}$$

Transforming the earlier equations into state variables, equation (1) is formulated as:

$$\frac{d_{iL1}}{dt} = \frac{V_g - v_{C1}}{L_1} \tag{5}$$

Similarly, we derive equation (2)

$$\frac{d_{iL2}}{dt} = \frac{v_{C1} - v_{C2}}{L_2} \tag{6}$$

Concerning equation (3),

$$\frac{d_{VC1}}{dt} = \frac{I_{L1} - I_{L2}}{C_1} \tag{7}$$

Lastly, to equation (4),

$$\frac{d_{VC2}}{dt} = \frac{I_{L2} - I_R}{C_2} \tag{8}$$

### B. REPRESENTATION OF THE EQUATIONS IN STATE OFF

Regarding the converter, as illustrated in Figure 2, the following equations are the OFF state of the quadratic Buck derived:

$$V_{L1} = -v_{C1} \tag{9}$$
$$V_{L2} = -v_{C2} \tag{10}$$
$$I_{L1} = -I_{C1} \tag{11}$$
$$I_{L2} = I_{C2} + I_R \tag{12}$$

When formulating the preceding equations (9 to 12) in terms of state variables, we obtain equation (9).

$$\frac{d_{iL1}}{dt} = \frac{-v_{C1}}{L_1} \tag{13}$$

For equation (10), the expression is as follows:

$$\frac{d_{iL2}}{dt} = \frac{-v_{C2}}{L_2} \tag{14}$$

In a parallel manner, equation (11) can be expressed as:

$$\frac{d_{VC1}}{dt} = \frac{i_{L1}}{C_1} \tag{15}$$

Lastly, for equation (12):

$$\frac{d_{VC2}}{dt} = \frac{i_{L2} - i_R}{C_2} \tag{16}$$

This section is reproduced from [43]

## III. QUADRATIC BUCK SWITCHED MODEL

The state variable equation is multiplied, yielding U in the ON state and (1)-U) in the OFF state.

For the inductor current ($\mathbf{I_{L1}}$) in this scenario, the state variable is determined through the following equation:

$$\frac{d_{iL1}}{dt} = \frac{V_g - v_{C1}}{L_1} * u + \frac{-v_{C1}}{L_1} * (1-u) \tag{17}$$

$$\frac{d_{iL1}}{dt} = \frac{V_g}{L_1} * u - \frac{v_{C1}}{L_1} \tag{18}$$

For the inductor current $I_{L2}$, the state variable is derived using the following equation:

$$\frac{d_{iL2}}{dt} = \frac{v_{C1} - v_{c2}}{L_2} * u + \frac{-v_{c2}}{L_2} * (1-u) \tag{19}$$

$$\frac{d_{iL2}}{dt} = \frac{v_{C1}}{L_2} * u - \frac{v_{c2}}{L_2} \tag{20}$$

For the variable $v_{C1}$, the expression is as follows:

$$\frac{d_{VC1}}{dt} = \frac{i_{L1} - i_{L2}}{C_1} * u + \frac{I_{L1}}{C_1} * (1-u) \tag{21}$$

$$\frac{d_{VC1}}{dt} = \frac{-i_{L2}}{C_1} * u + \frac{i_{L2}}{C_1} \tag{22}$$

The state variable v_C2 is acquired as follows:

$$\frac{d_{VC2}}{dt} = \frac{i_{L2} - i_R}{C_2} * u + \frac{i_{L2} - i_R}{C_2} * (1-u) \tag{23}$$

$$\frac{d_{VC2}}{dt} = \frac{i_{L2}}{C_2} * u - \frac{v_{c2}}{C_2 R} \tag{24}$$

This section is reproduced from [43].

## IV. AVERAGE MODEL QUADRATIC BUCK

Substituting the variable 'u' with 'd' and assigning the state equations as functions:

Regarding the variable $\mathbf{iL_1}$

$$f_1 = \frac{d_{iL1}}{dt} = \frac{V_g}{L_1} * d - \frac{v_{C1}}{L_1} \tag{25}$$

Concerning the variable $iL_2$

$$f_2 = \frac{d_{iL2}}{dt} = \frac{v_{C1}}{L_2} * d - \frac{v_{c2}}{L_2} \tag{26}$$

for $v_{C1}$ the expression is as follows:

$$f_3 = \frac{d_{VC1}}{dt} = \frac{-i_{L2}}{C_1} * d + \frac{i_{L1}}{C_1} \tag{27}$$

$$f_4 = \frac{d_{VC2}}{dt} = \frac{i_{L2}}{C_2} * d - \frac{v_0}{C_2 * R} \tag{28}$$

Setting the previously provided equations equal to zero results in the following:

$$f_1 = \frac{V_g}{I_1} * d - \frac{V_{C1}}{L_1} = 0 \tag{29}$$

Simplifying leads to:

$$V_g * D = V_{C1} \tag{30}$$

Concerning the function$f_2$

$$f_2 = \frac{V_{C1}}{I_2} * d - \frac{V_0}{L_2} = 0 \tag{31}$$

Streamlining:

$$f_2 = V_{C1} * D = V_0 \tag{32}$$

For, $f_3$, the expression is as follows:

$$f_3 = \frac{-I_{L2}}{C_1} * d + \frac{I_{L1}}{C_1} = 0 \tag{33}$$

Condensing:

$$I_{L2} * D = I_{L1} \tag{34}$$

Finally, concerning the function $f_4$:

$$f_4 = \frac{I_{L2}}{C_2} - \frac{V_{c2}}{C_2 * R} = 0 \tag{35}$$

By simplification, the formula is derived:

$$I_{L2} = \frac{V_0}{R} \tag{36}$$

This section is reproduced from [43].

## V. QUADRATIC BUCK LINEAR MODEL

primary goal, as per the model, is to yield the Transfer Function elucidating the system's behavior, resulting in the following matrix:

$$\frac{d}{dt} = \begin{bmatrix} i_{L1} \\ v_{C1} \\ i_{L2} \\ v_{C2} \end{bmatrix} = Ax + Bu$$

$$A = \begin{bmatrix} \frac{\partial}{\partial iL_1} f_1 & \frac{\partial}{\partial iC_1} f_1 & \frac{\partial}{\partial iL_2} f_1 & \frac{\partial}{\partial vC_2} f_1 \\ \frac{\partial}{\partial iL_1} f_2 & \frac{\partial}{\partial iC_1} f_2 & \frac{\partial}{\partial iL_2} f_2 & \frac{\partial}{\partial vC_2} f_2 \\ \frac{\partial}{\partial iL_1} f_3 & \frac{\partial}{\partial iC_1} f_3 & \frac{\partial}{\partial iL_2} f_3 & \frac{\partial}{\partial vC_2} f_3 \\ \frac{\partial}{\partial iL_1} f_4 & \frac{\partial}{\partial iC_1} f_4 & \frac{\partial}{\partial iL_2} f_4 & \frac{\partial}{\partial vC_2} f_4 \end{bmatrix} * \begin{bmatrix} i\hat{L}_1 \\ v\hat{C}_1 \\ i\hat{L}_2 \\ v\hat{C}_2 \end{bmatrix}$$

$$Bu = \begin{bmatrix} \frac{\partial}{\partial d} f_1 \\ \frac{\partial}{\partial d} f_2 \\ \frac{\partial}{\partial d} f_3 \\ \frac{\partial}{\partial d} f_4 \end{bmatrix} * \hat{d}Y = \begin{bmatrix} 0 & 0 & 0 & 1 \end{bmatrix} * \begin{bmatrix} i\hat{L}_1 \\ v\hat{C}_1 \\ i\hat{L}_2 \\ v\hat{C}_2 \end{bmatrix}$$

The formula for the transfer function is expressed as:

$$G(s) = Y * [SI - A]^{-1} * Bu \tag{37}$$

Solving equation 37, we arrive at the transfer function $G(s)$.

This section is based on the findings of [43]. Equation (38), as shown at the bottom of the next page.

## VI. QBC STATIC DESIGN

Inductances: The inductance value is determined based on the current ripple pattern within the coil, as illustrated in Figure 3. The equation for inductance when the system is in the ON state is depicted by the gradient of the line originating from 0 to $\boldsymbol{DT_s}$, while the slope between $\boldsymbol{DT_s}$ and $\boldsymbol{T_s}$ defines the coil current value in the OFF state.

$$\boldsymbol{m = \frac{\Delta Y}{\Delta X}} \tag{39}$$

Starting from this juncture, we can ascertain the individual values for each of the coils.

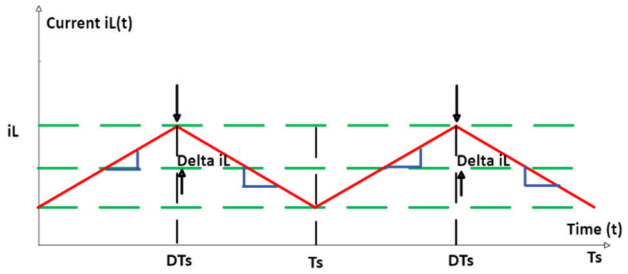


**FIGURE 3.** Voltage ripple delta across coils.

$L_1$: To compute this inductor, consult both equation (5) and equation (39), wherein:

$$\frac{V_g - v_{C1}}{L_1} = \frac{2 * \Delta I}{D * TS}$$

Solving for $L_1$: we get:

$$\frac{D * TS * (V_g - v_{C1})}{2 * \Delta I} \tag{40}$$

This can be simplified using equation (30):

$$L_1 = \frac{D * TS * V_g(1 - v_{C1})}{2 * \Delta I} \tag{41}$$

$\boldsymbol{L_1}$: To determine its value, the ON state is considered, as per equations (6) and (39).

$$\frac{v_{C1} - v_{C2}}{L_2} = \frac{2 * \Delta I}{D * TS}$$

Solving for $L_2$: we get:

$$L_2 = \frac{D * TS * (v_{C1} - v_{C2})}{2 * \Delta I} \tag{42}$$

By equation (32), the expression can be simplified to:

$$L_2 = \frac{D * TS * v_{C1}(1 - D)}{2 * \Delta I} \tag{43}$$

Capacitances: As depicted in Figure 4, an examination reveals that determining capacitance entails a current ripple shape with a slightly altered pattern, starting with a negative gradient. Likewise, the condition of the coil is affected by the ON state, as seen in Figure 3, where it is part of the OFF state. Here, the change is minimal, as it initiates with a negative gradient when the equation is multiplied by a lesser value, signifying a negative gradient like the slope calculation [43].

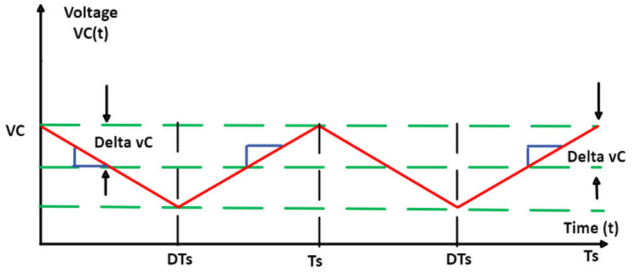


**FIGURE 4.** Capacitor ripple current.

$\boldsymbol{C_1}$: To ascertain the capacitance value for the capacitor $\boldsymbol{C_1}$, utilize the ON state, referencing both equation (7) and equation (39).

$$\frac{v_{C1} - v_{C2}}{L_2} = \frac{2 * \Delta I}{D * TS}$$

Determining $C_1$ through the equation:

$$C_1 = \frac{D * TS * (I_{L1} - I_{L2})}{2 * \Delta v_{C1}} \tag{44}$$

With the application of equation (34), the expression is simplified to:

$$C_1 = \frac{-D * TS * I_{L1}(1 - I_{L2})}{2 * \Delta v_{C1}} \tag{45}$$

$C_2$: To find out the capacitance value for the capacitor $C_2$ when it is in the ON state, refer to equation (8) and equation (39), where:

$$\frac{I_{L2} - I_R}{C_2} = \frac{2 * \Delta v_{C2}}{D * TS}$$

By solving the equation provided earlier for the capacitance of $C_2$ we arrive at:

$$C_2 = \frac{D * TS * (i_{L2} - i_R)}{2 * \Delta V_{C2}} \tag{46}$$

By applying equation (36), this expression can be simplified to:

$$C_2 = 0 \tag{47}$$

As the value of $\boldsymbol{C_2}$ cancels out, experimental demonstration confirms its correct interaction with the value of $\boldsymbol{C_1}$

$$G(s) = \frac{\left(\left(\frac{v_{C1}}{C_1C_2L_2}\right)\left(S^2 - \left(\frac{D_{IL1L1}}{V_{C1}}\right)S + \left(\frac{1}{L_1} + \frac{D_{vg}}{R_{C1}V_{C1}}\right)\right)\right)}{S^4 + \left(\frac{1}{RC_2}\right)S^3 + \left(\frac{D^2L_1 + L_2 - 2}{L_1L_2}\right)S^2 + \left(\frac{D^2L_1 + L_2}{C_1C_2L_1L_2R}\right)S + \left(\frac{1}{C_1C_2L_1L_2R}\right)} \tag{38}$$

### A. DUTY CYCLE ANALYSIS.

Deemed highly beneficial for controlling switched PWM signal sources during the process of turning the transistors on or off; to achieve this, equations (30) and (31) are compared and equated, yielding the following result:

$$V_g * D = \frac{v_0}{D} \tag{48}$$

clarifying $\boldsymbol{D}$:

$$D = \sqrt{\frac{v_0}{V_g}} \tag{49}$$

This section is based on the findings of [43].

## VII. PASSIVITY-BASED CONTROL PBC FOR DC POWER CONVERTERS

To develop the passivity-based controller, examine its energy modeling as outlined in [33]. Utilize a comprehensive average model inherent in certain quadratic topology DC converters, featuring the following structure.

$$\dot{A}x = \zeta\ (u_{av})\, x - Rx + bu_{av} + \varepsilon \tag{50}$$

Given that A represents a diagonal matrix with nonnegative entries, the symmetric matrix $\boldsymbol{\zeta\,(u_{av})}$ establishes a framework for every $\boldsymbol{u_{av}}$, featuring a directed function at input Uthat evaluates the system's conservative forces, represented by $\boldsymbol{\zeta 0 + \zeta u}$. The matrix R, which is nonnegative semidefinite, encompasses the aggregate damping terms present in circuit model B, together with a vector that includes terms for constant external forces, with these components dependent on external power sources. Furthermore, $\boldsymbol{\varepsilon}$captures fixed voltage levels sourced externally, as quantified by the vector x within the space $\boldsymbol{x \epsilon R_n}$.

Passive control adheres to the trajectory of the state denoted as $\boldsymbol{x^*(t)}$ based on the system's structure, employing a candidate Lyapunov function to regulate the output trajectory. This is accomplished by utilizing the segment error $e = (x - x_*(t))$, which is defined as:

$$v(e) = \frac{1}{2} e^T A_e = \frac{1}{2}(x - x^*(t))A(x - x^*(t)) \tag{51}$$

Its time derivative is:

$$\begin{aligned} \dot{v}\,(e) &= (\mathrm{x} - \mathrm{x}^*(\mathrm{t}))T\,\mathrm{A}(\dot{\mathrm{x}} - \dot{\mathrm{x}}^*(\mathrm{t})) \\ &= (\mathrm{x}) - \mathrm{x}^*\,(\mathrm{t})T\left([\zeta\ (u_{av}) - R]\, x + b + \varepsilon - A\dot{x}^*\,(t)\right) \end{aligned} \tag{52}$$

By rearranging, we obtain:

$$\begin{aligned} &A\dot{x} * (t)) \\ &= \zeta(u_{av})\mathrm{x}^*(\mathrm{t}) - R\mathrm{x}^*(\mathrm{t}) + bu_{av} + \varepsilon + RI(x - \dot{\mathrm{x}}^*(t)) \end{aligned} \tag{53}$$

With a segmented nonnegative symmetric matrix $RI$ that adheres to the given condition $R + RI > O$

Assessing the dynamic trajectory $\mathrm{e}^T \zeta(\mathrm{u})\mathrm{e} = 0$, for all u, considering the Lyapunov function V(e) and its time derivative

$$\begin{aligned} \dot{V}\ (\mathrm{e}) &= \mathrm{e}^{\mathrm{T}}\ (\zeta\ (\mathrm{u_{av}})\, \mathrm{e} - \mathrm{Re} - \mathrm{R_{Ie}}) = -\mathrm{e}^{\mathrm{T}}\ (\mathrm{R} + R_{\mathrm{I}})\, \mathrm{e} \\ &< 0 \end{aligned} \tag{54}$$

From a starting point of an asymptotically stable equilibrium, the error may exhibit exponential behavior toward its desired equilibrium. Therefore, it's important to ensure that the eigenvalues of $K_A \mathrm{Y}\ K_R + R_I$, are both nonnegative and symmetric, with $A\mathrm{y}\ R + R_I$having $K=$ equal to the minimum of $\{K_A \mathrm{Y}\ K_R + R_I\}$. Assess its stability by:

$$\dot{\mathrm{V}}\ (\mathrm{e}) = -\mathrm{e}^T\ (\mathrm{R} + R_I)\, \mathrm{e} - \mathrm{KV}\ (\mathrm{e}) \tag{55}$$

Therefore, the presence of the matrix RI combines stability characteristics with the damping matrix R, ensuring that R+RI > O serves as a dissipation criterion. This occurs because the setup of matrix $B$accomplishes feedback damping, resulting in the spaces $R_I$and $B$ not being inherently independent.

$$A\dot{x^*}(t) = \zeta\ (u_{av})\, x^*(t) - Rx^*(t) + bu_{av} + \varepsilon + R_I\left(x - x^*(t)\right) \tag{56}$$

The system under control and its supplementary damping:

$$R_I\left(x - x^*(t)\right) \tag{57}$$

Improves the initial dynamic behavior, whereas the error functions as a benchmark model demonstrating efficient energy dissipation. This leads to an ideal path for the output state when feedback is applied, given the conditions of a desired minimum phase output. The dynamics of the reference then become autonomous, defining the resilient controller.

### A. PASSIVITY-BASED CONTROL PBC

The standardized model provides a passive representation of both the average input $\boldsymbol{u_{av}}$ and the conductor's current $\boldsymbol{x_1}$. In the normalized averaged model, we make specific observations:

$$\begin{aligned} \dot{x_1} &= -x_2 + u_{av} \\ \dot{x_2} &= x_1 - u_{av}x_3 \\ \propto_1 \dot{x_3} &= u_{av}x_2 - x_4 \\ \propto_2 \dot{x_4} &= x_3 - \frac{1}{Q}x_4 \end{aligned} \tag{58}$$

The values of $\boldsymbol{x_4}$representing the parameterized equilibrium points of the output voltage are established by$\bar{\boldsymbol{x}}_{\boldsymbol{4}}$indicating:

$$\bar{x}_1 = \frac{\sqrt{x^4}^3}{Q}; \bar{x}_2 = \sqrt{\bar{x}_4}; \bar{x}_3 = \frac{\bar{x}_4}{Q} \tag{59}$$

The output voltage, represented as $x_4$, exhibits a non-minimum phase characteristic distinct from the inductor's current,$x_1$, which demonstrates a minimum phase output. Consequently, the output voltage indirectly affects the

inductor current $x_1$, moving it toward its equilibrium point. The total average energy stored in the converter is then expressed as:

$$H(x) = \frac{1}{2}\left({x_1}^2 + {x_2}^2 + \propto_1 {x_3}^2 + \propto_2 {x_4}^2\right) \tag{60}$$

The time derivative of $H(x)$is given by:

$$\dot{H}(x) = -\frac{1}{Q}{x_4}^2 + x_1 u_{av} \leq x_1 u_{av} \tag{61}$$

Describing a passive relationship between the average control input $u_{av}$, and both the recent and time integral H, is referred to as passive inequality, as outlined below:

$$H\,|x(t)| - H\,|x(o)| \leq \int_o^t x_1\,(\sigma)\,u_{av}\,(\sigma)\,d_\sigma \tag{62}$$

When feedback is utilized to dampen the system, an auxiliary system is introduced, employing:
$R_1\,(x_1 - x_{1d})\,, R_1 > o$ Therefore,

$$\begin{aligned} \dot{x_{1d}} &= -x_{2d} + u_{av} + R_1(x_1 - x_{1d}) \\ \dot{x_{2d}} &= x_{1d} - u_{av}x_{3d} \\ \propto_1 \dot{x_{3d}} &= u_{av}x_{2d} - x_{4d} \\ \propto_2 \dot{x_{4d}} &= x_{3d} - \frac{x_{4d}}{Q} \end{aligned} \tag{63}$$

Contemplating the normalized average error variables.

$$e_i = x_i - x_{id}, \quad i = 1, \ldots, 4.$$

The behavior of the error dynamical is described by:

$$\begin{aligned} \dot{e_1} &= -e_2 - R_1 e_1 \\ \dot{e_2} &= e_1 - u_{av}e_3 \\ \propto_1 \dot{e_3} &= u_{av}e_2 - e_4 \\ \propto_2 \dot{e_4} &= e_3 - \frac{1}{Q}e_4 \end{aligned} \tag{64}$$

Concerning the Lyapunov function derived from the error space acquired during the trajectory tracking with coordinates, $e = (e_1, e_2, e_3, e_4)$, it is necessary to:

$$H(e) = \frac{1}{2}(e_1^2 + e_2^2 + \propto_1 e_3^2 + \propto_2 e_4^2) \tag{65}$$

The derivative of the preceding non-negative function, where trajectory control induces a dynamic error, is expressed as:

$$(\dot{H}(\mathrm{e}) = -R_1 {\mathrm{e}_1}^2 - \frac{1}{\mathrm{Q}}{\mathrm{e}_4}^2 \leq 0 \tag{66}$$

Achieving the alignment of points within the error domain via $(\dot{H}(e) = 0$, leading to the intersection of hyperplanes at $e_1 = e_4 = 0$, thus resulting in $e_3 = 0$and $e_2 = 0$. According to Lasalle's theorem, the equilibrium state $e_i = 0$, for $i = 1 \ldots .4$, attains global asymptotic stability. Consequently, the trajectories of the system, represented by x(t), along with the auxiliary trajectories xd(t), exhibit asymptotic convergence. This facilitates the identification of the precise equilibrium value for the desired average inductor current $X_{1d}$within the dynamics of the auxiliary system. The auxiliary dynamic equation's control input, *Uav*, for the dynamic average feedback controller *Uav* is derived as follows:

$$\begin{aligned} u_{av} &= \xi_2 - R_1(x_1 - \overline{\mathrm{x_1}}) \\ \xi_2 &= \overline{\mathrm{x_1}} - u_{av}\xi_3 \\ \propto_1 \xi_3 &= u_{av}\xi_2 - \xi_4 \\ \propto_2 \xi_4 &= \xi_3 - \frac{1}{Q}\xi_4 \end{aligned} \tag{67}$$

Variables $\xi_2, \xi_3 y \xi_4$constitute the dynamic state controller. Finally, by integrating the auxiliary state $x_{2d}, x_{3d} and x_{4d}$which will subsequently replace the auxiliary dynamic model, it is necessary to:

$$x_{1d} = \overline{\mathrm{x_1}} \tag{68}$$

The control signal $u_{av}$acts as the estimated dynamic closed-loop derivative for the control system, derived from the scaled estimate of the input or primary current $x_1$, influencing the dynamic closed-loop response of the control system. The $A\Sigma - \Delta$modulator is utilized to deliver the $u_{av}$input to the switched model, implementing the estimated closed-loop control strategy.

### B. VALUES FOUND IN THE SIMULATIONS

In the context of a parameterized converter, characterized by the following:

**TABLE 1. Values of QBC parameters.**

| $L_1$ | $L_2$ | $C_1$ | $C_2$ | $R$ | $E$ |
|---|---|---|---|---|---|
| $1{,}2mH$ | $250\mu H$ | $200\mu f$ | $100\mu f$ | $4.7\Omega$ | $380v$ |

**TABLE 2. Parameters for the desired voltage.**

| $Q_{L1}$ | $Q_{L2}$ | $\alpha_1$ | $\alpha_2$ | $\overline{v_2} = Vd$ |
|---|---|---|---|---|
| $40.9480x10^{-3}$ | 1.29489 | 1 | 1 | $48v$ |

**TABLE 3. Variable values for the QBC.**

| $\overline{i_1}$ | $\overline{v_1}$ | $\overline{i_2}$ | $\overline{U_{av}}$ |
|---|---|---|---|
| $3{,}7022A$ | $135.05v$ | $10{,}4167A$ | $\sqrt{48.}$ |

Achieving normalized values is feasible under the following condition: $Q = R\sqrt{\frac{C}{L}}$.

Steady-state values for other missing state variables are listed below in Table 3.

The closed-loop passivity-based stabilization is the approach executed using a $\Sigma - \Delta$ modular system, this aligns with the average passivity controller. This controller

characterizes the average response of the system by utilizing techniques derived from the energy-based model and adjusted based on the system's damping.

### C. ACCURATE ERROR DYNAMICS PASSIVE OUTPUT FEEDBACK CONTROL

The accurate depiction of the dynamic model of stabilization error within the average system model follows the framework influenced by the energy-based error dynamics, specifically oriented towards the generalized Hamiltonian form. Its response in this scenario demonstrates passivity in the stabilization error dynamics.

Its primary attribute lies in generating straightforward linear feedback, possessing time invariance. This feedback transforms an asymptotically and globally stable point integrated into a closed-loop system, structurally dissipated to adjust to the system.

### D. RESULTS ACHIEVED

The comprehensive normalized model of the DC-DC QBC expressed in a generalized Hamiltonian canonical form can be illustrated as:

$$\ddot{x} = \zeta\,(u_{av})\,\frac{\partial H}{\partial x} - R\frac{\partial H}{\partial e} + bu_{av} + \gamma \tag{69}$$

As $\mathscr{H}(\S)$ denotes the system's energy, described as $\mathscr{H}(\mathrm{x})=\frac{1}{2}\boldsymbol{x}^{\boldsymbol{T}}\boldsymbol{x}$, here, the partial derivative of $\mathscr{H}$ respect to x is equal to x, $\partial\mathscr{H}/\partial x = x$ and the matrix $\boldsymbol{\zeta}\,(\boldsymbol{u_{av}})$is not orthogonal. R is a non-negative symmetric matrix, and the vector b remains unchanged, while $\varepsilon$ represents the external input to the system.

$$\zeta\,(u_{av}) = \begin{bmatrix} 0 & -1 & 0 & 0 \\ 1 & 0 & -u_{av} & 0 \\ 0 & u_{av} & 0 & -1 \\ 0 & 0 & 1 & 0 \end{bmatrix}, b = \begin{bmatrix} 1 \\ 0 \\ 0 \\ 0 \end{bmatrix}, \varepsilon = 0 \tag{70}$$

For a linear converter, the matrix $\boldsymbol{\zeta}\,(\boldsymbol{Uav})= \boldsymbol{\zeta}$ remains unchanged. However, within the framework of the nonlinear QBC $\boldsymbol{\zeta}\,(\boldsymbol{Uav})$is symmetrically adjusted based on the average control input $\boldsymbol{Uav}$, It can be stated that $\boldsymbol{\zeta}\,(\boldsymbol{Uav})$maintains its constant values doverline $\overline{\overline{\boldsymbol{U}}}$,utilizing the expansion property.

$$\zeta\,(u_{av}) = \zeta\,(\bar{u}) + \left.\frac{\partial\zeta\,(u_{av})}{\partial u_{av}}\right|_{u_{av}=\bar{U}} (u_{av} - \bar{u}) \tag{71}$$

By the definition of $\boldsymbol{\zeta}\,(\boldsymbol{u_{av}})$ it signifies a dependency on $\boldsymbol{u_{av}}$, implying that the matrix $\frac{\boldsymbol{\partial\zeta\,(u_{av})}}{\boldsymbol{\partial u_{av}}}$ is constant and exhibits symmetrical biases. Consequently, the equations at the equilibrium point demonstrate the following behavior:

$$\boldsymbol{0 = \zeta\,(g)\,\frac{\partial H}{\partial x}|_{x=x} - R\frac{\partial H}{\partial x}|_{x=x} + bu + \mathcal{E}} \tag{72}$$

$$0 = \zeta(u)x - Rx + bu + \mathcal{E} \tag{73}$$

Viewing $\bar{x}$ as a fixed steady-state approximation and the average output control $\bar{u}$ as a constant ranging from $\bar{u} \in [0, 1]$ the introduction of stabilization errors leads to:

$$e = x - \bar{\mathrm{x}},\ \mathrm{e_u} = \mathrm{u_{av}} - \bar{\mathrm{u}}$$

henceforth,

$$e = x - \bar{x} = \frac{\partial H(x)}{\partial x} - \frac{\partial H(\overline{x})}{\partial(\bar{x})} = \frac{\partial H(e)}{\partial e} \tag{74}$$

so,

$$\dot{e} = \dot{x}$$

At this point, it can be observed that the stabilization error dynamics adhere to a general satisfaction:

$$\dot{e} = \zeta\,(u_{av})\,\frac{\partial H(e)}{\partial e} - R\frac{\partial H\,(e)}{\partial e} + be_u + [\frac{\partial\zeta\,(u_{av})}{\partial u_{av}}\frac{\partial H\,(x)}{\partial x}|_{x=\bar{\mathrm{x}}}]e_u$$

*Then,*

$$\dot{e} = \zeta\,(u_{av})\,e - Re + [b + \frac{\partial\zeta(u_{av})}{\partial u_{av}}\bar{x}]e_u \tag{75}$$

Differentiating the equation yields:

$$\dot{e} = \zeta\,(u_{av})\,\frac{\partial H\,(e)}{\partial e} - R\frac{\partial H\,(e)}{\partial e} + be_u + \varepsilon + \zeta\,(u_{av})\,\frac{\partial H}{\partial x}|_{x=\bar{\mathrm{x}}} - R\frac{\partial H}{\partial x}|_{x=\bar{\mathrm{x}}} + b\bar{\mathrm{u}} \tag{76}$$

Utilizing the equilibrium relations results in:

$$0 = \varepsilon + \zeta\,(\bar{\mathrm{u}})\,\frac{\partial H\,(e)}{\partial x}|_{x=\bar{\mathrm{x}}} - R\frac{\partial H}{\partial x}|_{x=\bar{\mathrm{x}}} + b\bar{\mathrm{u}} \tag{77}$$

Therefore, it satisfies:

$$\dot{e} = \zeta\,(u_{av})\,\frac{\partial H(e)}{\partial e} - R\frac{\partial H\,(e)}{\partial e} + be_u + [\zeta\,(u_{av}) - \zeta(\bar{u})]\,\frac{\partial H}{\partial x}|_{x=\bar{x}} \tag{78}$$

Thus

$$\dot{e} = \boldsymbol{\zeta\,(u_{av})\,e - Re + be_u}\frac{\boldsymbol{\partial\zeta\,(u_{av})}}{\boldsymbol{\partial u_{av}}}\bar{x}\left[\frac{\boldsymbol{\partial H}}{\boldsymbol{\partial x}}|_{\boldsymbol{x=\bar{x}}}\right]\boldsymbol{e_u} \tag{79}$$

so,

$$\dot{e} = \zeta\,(u_{av})\,e - Re + be_u + \frac{\partial\zeta\,(u_{av})}{\partial u_{av}}\bar{x}e_u \tag{80}$$

clarifying,

$$\dot{e} = \zeta\,(u_{av})\,e - Re + [b + \frac{\partial\zeta\,(u_{av})}{\partial u_{av}}\bar{\mathrm{x}}]e_u \tag{81}$$

To ensure the stability of the dynamic error, it is essential to consider the following:

As per the definition, $\boldsymbol{\zeta\,(u_{av})\,e} = \zeta\,(u_{av})\,\frac{\partial H(e)}{\partial e}$represents the conservative nonlinear term and the subsequent definition is linked to $\boldsymbol{u_{av}}$ The provided definition below is associated with:

$$\boldsymbol{e^T\zeta\,(u_{av})\,e} = \frac{\boldsymbol{\partial H(e)}}{\boldsymbol{\partial e^T}}\boldsymbol{\zeta\,(u_{av})}\frac{\boldsymbol{\partial H(e)}}{\boldsymbol{\partial e}} = \boldsymbol{0} \tag{82}$$

Irrelevant to the stability of the closed-loop input system $\boldsymbol{e_u} = \boldsymbol{u} - \bar{\mathrm{u}}$ in a manner such that $\boldsymbol{-Re + be_u} + \frac{\boldsymbol{\partial\zeta(u_{av})}}{\boldsymbol{\partial u_{av}}}\bar{\mathrm{x}}\boldsymbol{e_u}$, represents The inverse of this pertains to the dynamic error analysis, which includes both the linearization along the tangent and the non-linearization of the matrix. $\boldsymbol{\zeta}(Uav)$ Subsequently, the

system progresses, $\dot{x}= \zeta\ (\boldsymbol{u_{av}})\ \frac{\partial \boldsymbol{H}}{\partial \boldsymbol{x}} - \boldsymbol{R}\ \frac{\partial \boldsymbol{H}}{\partial \boldsymbol{x}} + \boldsymbol{bu_{av}} + \varepsilon$ around the break-even point where $x = \bar{x}$, $u_{av} = \bar{u}$

$$\dot{x}\delta = \zeta\ (\bar{u})\, x\delta - Rx\delta + bu\delta + \frac{\zeta\ (u_{av})}{\partial u_{av}} \bar{x} u\delta x\delta = x - \bar{x} \quad (83)$$

Examining the three terms governing error dynamics within the right half-plane, shaping the error dynamics for system stabilization and its correspondence $\boldsymbol{x\delta} = \boldsymbol{x} - \bar{x}$ with e and $\boldsymbol{u\delta} = \boldsymbol{u_{av}} - \bar{\boldsymbol{u}}$ incorporating $\boldsymbol{e_u}$.

The principle underlying linear incremental feedback is crucial for the formulation of a controller that stems from the objective of achieving zero stabilization. This approach utilizes the model of average tangent stabilization to guide the system toward a specified equilibrium state, starting from an initial condition. To accomplish this, the control strategy makes use of referring to the average linear incremental feedback, it represents a linearized feedback method obtained from the tangent linearization of the model. This approach confirms the nonlinear equilibrium state as either semi-globally or asymptotically stable.

$$e_u = u_\delta = -k^T e = -k^T x_\delta \quad (84)$$

In the pursuit of stabilization, the poles of the averaged tangent linearization dynamics are illustrated as follows: Consider $k_T$ In the form of a row vector, it includes coefficients that offer feedback on the stabilization errors of the state [33]. The equation for the dynamics of the system error is then expressed as:

$$\dot{e} = \zeta\ (u_{av})\, e - Re - [b + \frac{\partial \zeta\ (u_{av})}{\partial u_{av}} \bar{x}] k^T e \quad (85)$$

$$\dot{e} = \zeta\ (u_{av})\, e - [R + \left( b \frac{\partial \zeta\ (u_{av})}{\partial u_{av}} \bar{\mathrm{x}} \right) k^T] e \quad (86)$$

Thus,

$$M = [R + \left( b + \frac{\partial \zeta\ (u_{av})}{\partial u_{av}} \bar{\mathrm{x}} \right) k^T] e \quad (87)$$

In this scenario, the eigenvalues of matrix $M$are located on the right side of the complex plane. However, it's important to note that $M$ is neither symmetric nor skew-symmetric.

$$M = \zeta M + RM \quad (88)$$

Containing the asymmetric$\zeta M$ and the symmetric $Rm$ is characterized as negative. $-Rm$.

$$M = \frac{1}{2} \left[ M - M^T \right] + \frac{1}{2} [M + M^T] \quad (89)$$

From there, we derive the system's closed-loop configuration:

$$\dot{e} = [\zeta\ (Uav) - \zeta M]\, e - [R + RM]\, e \quad (90)$$

The achievement of semi-global stability in the closed-loop system is a result of the inherent symmetry bias within the matrix.$\zeta\ (u_{av}) - \zeta M$for $u_{av}$, and additionally, from the symmetric matrix $R + R$M, as stipulated by the theorem previously outlined. It's noteworthy that the stability of averaged converters is characterized by non-linearity, attributed to the linear feedback. This linear feedback, in turn, contributes to the semi-global stabilization of nonlinear models in average conversion. The implementation of the closed-loop system involves the utilization of positive incremental output, all of which is incorporated within the framework of the standard model.

$$\begin{aligned} \dot{x_1} &= -x^2 + Uav \\ \dot{x_2} &= x_1 - Uav x_3 \\ \propto_1 \dot{x_3} &= Uav\, x_2 - x_4 \\ \propto_2 \dot{x_4} &= x_3 - \frac{1}{Q} x_4 \end{aligned} \quad (91)$$

Guiding the trajectories towards a stable average state equilibrium point to achieve the equilibrium voltage as the desired output.

$$\bar{x_4} = V_d, \text{by} \bar{x_1} = \frac{(vd)^{3/2}}{Q}, \bar{x_2} = \sqrt{vd}, \bar{x_3} = \frac{vd}{Q}, Uav = \sqrt{vd}$$

Establishing a connection from the state coordinates to the error space of stabilization reveals that:

$$\begin{aligned} e_1 &= x_1 - \frac{(vd)^{3/2}}{Q}, e_2 = x_2 - \sqrt{vd}, \\ e_3 &= x_3 - \frac{vd}{Q}, e_4 = x_4 - vd \end{aligned}$$

What dictates the correlation:

$$\begin{aligned} \dot{e_1} &= -e_2 + (Uav - \sqrt{vd}) \\ \dot{e_2} &= e_1 - Uave_3 - \frac{vd}{Q}(Uav - \sqrt{vd}) \\ \propto_1 \dot{e_3} &= Uave_2 - e_4 + \sqrt{vd}(Uav - \sqrt{vd}) \\ \propto_1 \dot{e_4} &= e_3 - \frac{1}{Q} e_4 \end{aligned} \quad (92)$$

Transitioning from the energy function to the error:

$$H(e) = \frac{1}{2} e^t A e = \frac{1}{2} \left[ {e_1}^2 + {e_2}^2 + \alpha_1 {e_3}^2 + \alpha_2 {e_4}^2 \right]$$

The matrix transpose is represented by:

$$A = A^T = diag(1, 1, \alpha_1, \alpha_2), e = \left[ e_1, e_2, e_3, e_4 \right]^T$$

This implies that:

$$\frac{\partial \mathrm{H(e)}}{\partial \mathrm{e}} = \mathrm{Ae} = \left[ \mathrm{e_1, e_2, x_1, e_3, x_2, e_4} \right]^{\mathrm{T}} \quad (93)$$

In the generalized Hamiltonian form, when the closed-loop system is employed, the computation of the error stabilization system occurs.

$$\begin{aligned} \dot{e} = & \begin{bmatrix} 0 & -1 & 0 & 0 \\ 1 & 0 & -\frac{1}{\alpha_1} Uav & 0 \\ 0 & \frac{1}{\alpha_1} Uav & 0 & -\frac{1}{\alpha_1 \alpha_2} \\ 0 & 0 & \frac{1}{\alpha_1 \alpha_2} & 0 \end{bmatrix} \frac{\partial H(e)}{\partial e} \\ & - \begin{bmatrix} 0\,0\,0 & 0 \\ 0\,0\,0 & 0 \\ 0\,0\,0 & 0 \\ 0\,0\,0 & \frac{1}{\alpha_2^2 Q} \end{bmatrix} \frac{\partial H\ (e)}{\partial e} + \begin{bmatrix} 1 \\ -\frac{\sqrt{d}}{Q} \\ \frac{\sqrt{vd}}{\alpha_1} \\ 0 \end{bmatrix} eUav \end{aligned} \quad (94)$$

where, $e_{Uav}$ can be represented as follows:

$$e_{Uav} = Uav - \sqrt{ud} \tag{95}$$

The depiction of error stabilization using the Hamiltonian method, integrated within the passive output, is expressed as:

$$e_y = \frac{bT\partial H(e)}{\partial e} = e_1 - \frac{vd}{Q}e_2 + \sqrt{vd}e_3 \tag{96}$$

Nevertheless, it is conceivable to validate the adjustment of dispersion, which, in this instance, is not entirely met, as:

$$\begin{aligned}\dot{H}(e) &= -\frac{\partial H(e)}{\partial eT}[R + \gamma bbT]\frac{\partial H(e)}{de} \\ &= \left[-e^T \mathrm{A}\left[R + \gamma, bb^T\right]\right]\mathrm{A}e, \leq 0\end{aligned} \tag{97}$$

Thus:

$$\begin{aligned}&A\left[R + Ybb^T\right]A \\ &= \begin{bmatrix} Y & -\gamma\frac{vd}{Q} & \gamma\sqrt{vd} & 0 \\ -\gamma\frac{vd}{Q} & \gamma\frac{v^2d}{Q^2} & -\gamma\frac{(vd)^{\frac{3}{2}}}{Q} & 0 \\ \gamma\sqrt{vd} & -\gamma\frac{(vd)^{\frac{3}{2}}}{Q} & Yvd & 0 \\ 0 & 0 & 0 & \frac{1}{Q} \end{bmatrix} \geq 0\end{aligned} \tag{98}$$

One might argue that the proximity of these vectors forms the null space of the matrix mentioned earlier, given that:

$$\begin{aligned}&z = [\boldsymbol{e_1}\ \boldsymbol{e_2}\ \boldsymbol{e_3}\ \boldsymbol{0}]\ \text{So,} \\ &\boldsymbol{\xi\delta} = \boldsymbol{e_1} - \frac{\boldsymbol{vd}}{\boldsymbol{Q}}\boldsymbol{e_2} + \sqrt{\boldsymbol{vd}}\boldsymbol{e_3} = \boldsymbol{0}\end{aligned} \tag{99}$$

Inside a subset of $\boldsymbol{R^4}$characterized by $\boldsymbol{ey} = \xi\delta$, hence, within this subset, the non-linear system is controlled by the equilibrium input $\boldsymbol{Uav} = \sqrt{\boldsymbol{vd}}$,with the error being maintained at $\boldsymbol{e_{Uav}} = \boldsymbol{0}$, This follows a direct trajectory in the error system where $\boldsymbol{e_y} = \boldsymbol{0}$and $\boldsymbol{e_{Uav}} = \boldsymbol{0}$

Therefore, according to Lasalle's asymmetric stability theorem, the closed-loop mean error system must demonstrate a highly stable equilibrium at its origin. This is accomplished through a series of paths originating from the point where $|\boldsymbol{e}|\left\{\dot{\boldsymbol{H}}(\boldsymbol{e}) = \boldsymbol{0}\right\}$ all controlled by the feedback-controlled average error system, thus establishing a highly stable equilibrium.

For this purpose, the feedback controller is defined as:

$$e_{Uav} = -\gamma ey = -\gamma\left[e_1 - \frac{vd}{Q}e_2 + \sqrt{vd}e_3\right] \tag{100}$$

Hence, the feedback control for average stabilization is characterized by the passive output:

$$\begin{aligned}Uav = \sqrt{vd} - Y\Bigg[&\left(x_1 - \frac{(vd)^{\frac{3}{2}}}{Q}\right) - \frac{vd}{Q}\left(x_2 - \sqrt{vd}\right) \\ &+\sqrt{vd}\left(x_3 - \frac{vd}{Q}\right)\Bigg]\end{aligned} \tag{101}$$

The output feedback demonstrates progressive passivity, with the initial controller feedback being tangential [33]. The stabilization response transitions to employing linear static passivity from the feedback controller.

Contemplating the determined parameters for the quadratic Buck switch described in Tables 1, 2, and table 3.

The key results of the switched system stem from the static controller based on linear passivity, because of the passive output arising from the precise dynamics of the stabilization error.

This section is based on the findings of [43].

## VIII. QUADRATIC BUCK CONTROLLER DESIGN USING CANONICAL FORMS

By employing state feedback and adopting the controllable and observable Canonical form, the behavior of the closed-loop system demonstrates consistent nonlinear dynamics through the utilization of differential algebra, leading to the generation of standardized current and voltage outputs [34].

### A. CONTROLLER DESIGN

The variable x denotes the normalized output current, which is associated with the voltage output relative to the output capacitor and the corresponding coil current.

Coming back to the standardized model:

$$\begin{aligned}\dot{x_1} &= -x_2 + Uav \\ \dot{x_2} &= x_1 - Uavx_3 \\ \propto_1 \dot{x_3} &= Uavx_2 - x_4 \\ \propto_2 \dot{x_4} &= x_3 - \frac{x_4}{Q} \\ y &= x_1\end{aligned} \tag{102}$$

Serving as one of the output dimensions for the entire system, a state coordinate transformation is executed with the invertible input as the independent variable.

$$\begin{aligned}&\begin{bmatrix} z_1 \\ z_2 \\ z_3 \\ z_4 \end{bmatrix} = \emptyset(x) = \begin{bmatrix} h_{(x)} \\ \dot{h}_{(x)} \\ \ddot{h}_{(x)} \\ h^{(3)}_{(x)} \end{bmatrix} \\ &= \begin{bmatrix} x_1 \\ Uav - x_2 \\ \dot{U}av - Uavx_3 - x_1 \\ \ddot{U}av + x_3\dot{U}av + \frac{1}{a1}(Uavx_2 - x_4 - \propto_1) Uav + x_2 \end{bmatrix}\end{aligned} \tag{103}$$

In this context, it pertains to the inverse transformation.

$$\begin{bmatrix} \boldsymbol{x_1} \\ \boldsymbol{x_2} \\ \boldsymbol{x_3} \\ \boldsymbol{x_4} \end{bmatrix} = \boldsymbol{\emptyset^{-1}}(\boldsymbol{Z}) \tag{104}$$

Thus, the dynamics regarding a desired average reference equilibrium for the output are outlined as follows:

$$Uav^{(3)} + \left(\frac{\bar{z_1}}{Uav} - \frac{3}{Uav}Uav + \frac{1}{\propto_2 Q}\right)\ddot{U}av + \frac{2}{U^2av}\dot{u}^3_{av} - \left(\frac{2\bar{z_1}}{U^2_{av}} + \frac{1}{\propto_2 UavQ}\right) + \left(2\frac{U^2_{av}}{\propto_1} + \frac{1}{a_1 \propto_2} + \frac{\bar{z}_1}{\propto_2 UavQ}\right) \dot{U}av + \frac{1}{\propto_1 \propto_2}\left(\frac{u^3av}{Q} - \bar{z_1}\right) = 0 \quad (105)$$

The equilibrium states of the zero dynamics are determined by the roots of the polynomials.

$$P\,(Uav) = \frac{1}{\propto_1 \propto_2}\left(\frac{u^3av}{Q} - \bar{z_1}\right) \quad (106)$$

In a manner that the provided equilibrium points:

$$Uav = \sqrt[3]{Q}z_1, Uav = \frac{1}{2}\sqrt[3]{Q}z_1(1 \pm \sqrt{3}\mathrm{i}) \quad (107)$$

where $Uav = \sqrt[3]{Q}z_1$introduces an unconventional phase diagram, and by employing the Lyapunov function, it is established to be asymptotically stable within its zero dynamics.

### B. CLOSED LOOP CONTROLLER DESIGN

The model is defined as:

$$\dot{z_1} = z_2; \dot{z_2} = z_3; \dot{z_3} = z_4; y = z_1$$
$$\dot{z_4} = Uav^3 + x_3\ddot{u}av + \frac{3Uavx_2 - 2x_4 - \propto_1}{\propto_1}\dot{U}av + \frac{\left(U^2av + \propto_1\right)(x_1 - Uavx_3)}{\propto_1} + \frac{x_4 - Qx_3}{\propto_1 \propto_2 Q}Ua \quad (108)$$

The inverse transformation yields the state vector comprised of $(x_1, x_2, x_3, x_4)$ The rate of change of $\dot{z_4}$ s computed as the average closed-loop dynamic linearization, represented by $Uav$

$$\dot{z_1} = z_2; \dot{z_2} = z_3; \dot{z_3} = z_4; \dot{z_4} = Uav; y = z_1 \quad (109)$$
$$Uav = Uav^3 + x_3\ddot{u}av + \frac{3Uavx_2 - 2x_4 - \propto_1}{\propto_1}\dot{U}av + \frac{\left(U^2av + \propto_1\right)(x_1 - Uavx_3)}{\propto_1} + \frac{x_4 - Qx_3}{\propto_1 \propto_2 Q}Uav \quad (110)$$

Deriving the equilibrium points in $\bar{z} = (\bar{z_1}, 0, 0, 0)$ by converging the trajectories to the equilibrium point z, $Uav$ is defined as follows:

$$Uav = -B_4Z_4 - B_3Z_3 - B_2Z_2 - B_1\left(Z_1 - \bar{Z_1}\right) \quad (111)$$

Consequently, the average closed-loop system is:

$$\begin{bmatrix}\dot{z_1}\\ \dot{z_2}\\ \dot{z_3}\\ \dot{z_4}\end{bmatrix} = \begin{bmatrix}0 & 1 & 0 & 0\\ 0 & 0 & 1 & 0\\ 0 & 0 & 0 & 1\\ -\beta_1 & -\beta_2 & -\beta_3 & -\beta_4\end{bmatrix} = \begin{bmatrix}z_1 - \bar{z_1}\\ z_2 - \bar{z_2}\\ z_3 - \bar{z_3}\\ z_4 - \bar{z_4}\end{bmatrix} \quad (112)$$

Thus, the polynomial defining the system is as follows:

$$P\,(s) = S4 + \beta_4 S^3 + \beta_3 S^2 + \beta_2 S + \beta_1 \quad (113)$$

Utilizing Ruth Hurwitz's method yields the desired polynomial pd(s) Subsequently, the coefficients Pd(s). are calculated and selected based on determining the stability roots. This selection is made by observing and characterizing the behavior of variables in the complex left half-plane.

$$Pd\,(s) = \left(s^2 + 2\xi_1 wn_1 s + w^2 n_1\right)\left(s^2 + 2\xi_2 wn_2 s + w^2 n_2\right) = s^4 + 2\left(\xi_1 wn_1 + \xi_2 wn_2\right)s^3 + \left(w^2 n_1 + 4\xi_1\xi_2 wn_1 wn_2 + w^2 n_2\right)s^2 + 2\left(\xi_1 wn_1 w^2 n_2 + \xi_2 w^2 n_1 wn_2\right)s + w^2 n_1 w^2 n_2 \quad (114)$$

The closed-loop gains of the system are determined by equating the coefficients of the polynomial.

$$\beta_1, \beta_2, \beta_3, \beta_4.$$
$$\beta_1 = w^2 n_1 w^2 n_2$$
$$\beta_2 = 2(\xi_1 wn_1 w^2 n_2 + \xi_2 w^2 n_1 wn_2)$$
$$\beta_3 = (wn_1^2 + 4\xi_1\xi_2 wn_1 wn_2 + w^2 n_2)$$
$$\beta_4 = 2(\xi_1 wn_1 + \xi_2 wn_2) \quad (115)$$

By equalizing, the stabilization of the system is achieved through:

$$Uav^{(3)} = -\beta_4 Z_4 - \beta_3 Z_3 - \beta_2 Z_2 - \beta_1\left(Z_1 - \bar{Z_1}\right) - X_3\ddot{U}av - \frac{3UavX_2 - 2X_4 - \propto_1}{\propto_1}\dot{U}av - \frac{\left(u^2av + \propto_1\right)(\propto_1 - UavX_3)}{\propto_1} - \frac{X_4 - QX_3}{\propto_1 \propto_2 Q}Uav \quad (116)$$

The state variables involved in the simulations are:

$$\mu_1 = Uav, \mu_2 = \dot{U}av, \mu_3 = \ddot{U}av \quad (117)$$

Formulating the controller using these state variables results in:

$$\dot{\mu_1} = \mu_2$$
$$\dot{\mu_2} = \mu_3$$
$$\dot{\mu_3} = -\beta_4 Z_4 - \beta_3 Z_3 - \beta_2 Z_2 - \beta_1\left(Z_1 - \bar{Z_1}\right) - X_3\mu_3 - \frac{3\mu_1 X_2 - 2X_4 - \propto_1}{\propto_1}\mu_2 - \frac{\left(\mu_1^2 + \propto_1\right)(X_1 - \mu_1 X_3)}{\propto_1} - \frac{X_4 - QX_3}{\propto_1 \propto_2 Q}\mu_1 \quad (118)$$

Replacing,

$$Z_1, Z_2, Z_3 y Z_4$$
$$Z_1 = x$$
$$Z_2 = \mu_1 - X_2$$
$$Z_3 = \mu_2 + \mu_1 X_3 - X_1$$
$$Z_4 = \mu_3 + \mu_2 X_3 - \frac{1}{X_1}\left(\mu_1 X_2 - X_4 - \propto_1\right)\mu_1 + X_2 \quad (119)$$

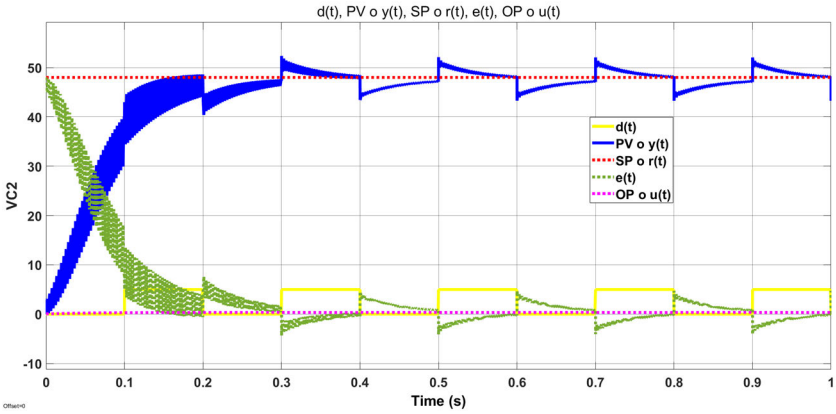


**FIGURE 5.** Validation of the response output $V_{C2}$ and its control components under disturbance.

Results of Simulations: Implemented utilizing the $\Sigma - \Delta$ modulator as per MATLAB simulations. $\Sigma - \Delta$ illustrates the output voltage, Taking into consideration the following parameters of the QBC:

The steady-state voltage is represented by the variables determined in table 4

**TABLE 4.** Principal QBC parameter values.

| $\overline{X_1}$ | $\overline{i_2}$ | $\overline{X_3}$ | $\overline{v_2}$ | $\overline{X_4}$ | $\overline{X_2}$ |
|---|---|---|---|---|---|
| $3{,}7022A$ | $10{,}4167A$ | $135.05v$ | $48v$ | 0,25 | $\sqrt{48}$ |

Figure 5 depicts the result of implementing a passivity-based control (PBC) algorithm alongside a Proportional-Integral (PI) adjustment on its output. This control strategy employs a PI method to regulate the current of the inductor and stabilize the voltage of the capacitor near the desired reference level.

The disturbance function, represented by the yellow line d(t), is depicted using step blocks. These blocks transition from 5 to zero and from zero to -5. At times, the disturbance function is substituted utilizing a square wave pulse generator, the blue line y(t) signifies the controlled variable or system output, adjusted to attain a 48-volt output. Meanwhile, the red line r(t) indicates the setpoint or the desired reference value. The red line r(t) represents the setpoint or desired reference value. The error signal, denoted by the green line e(t), is also shown.

Finally, the input signal to the system, represented by the violet line u(t), serves as the controlled pulse signal.

Given Considering the MCC and the operational states of the system response for stability, Figure 5 below illustrates the $V_{C1}$ response extracted from Figure 6, and Figure 7 illustrates the current $I_{L1}$.

For $V_{C2}$, the response is depicted in Figure 8. While it doesn't quite reach the expected value, the response closely approximates it. In this scenario, the delta is:

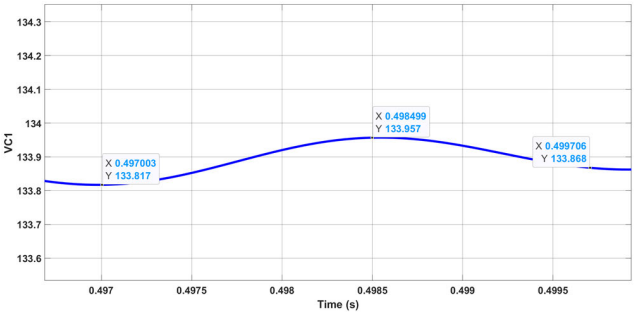


**FIGURE 6.** MATLAB simulation of $v_{C1}$ in.

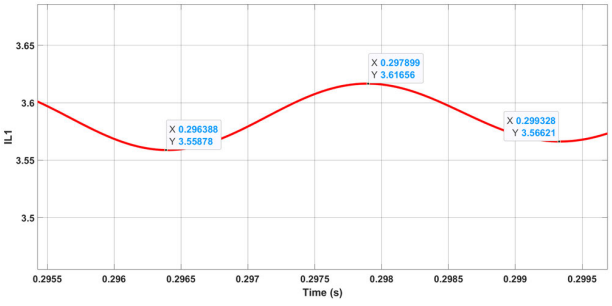


**FIGURE 7.** MATLAB simulation of $I_{L1}$.

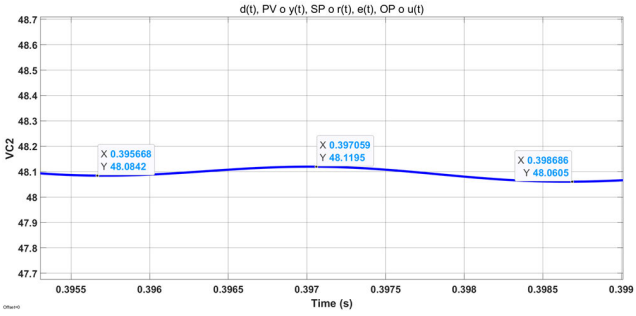


**FIGURE 8.** MATLAB simulation of $V_{C2}$.

Finally, Figure 9 illustrates the value of $\Delta_{IL2}$.

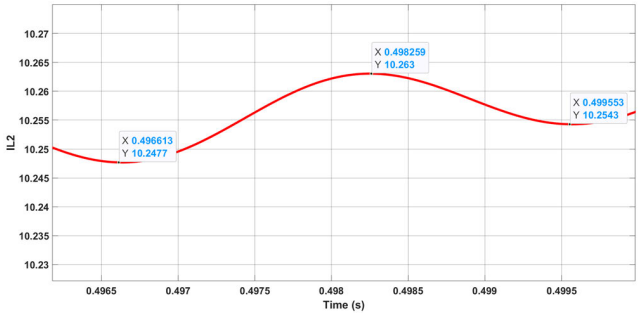


**FIGURE 9.** MATLAB simulation of $I_{L2}$.

The resultant response derived from the simulation of the system in a passive closed-loop configuration is also noticeable.

Employing a pulse generator set at a consistent 5 VDC amplitude, whereby disturbances undergo identical criteria for graph validation.

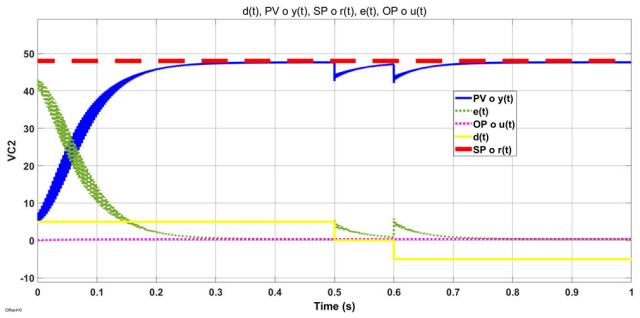


**FIGURE 10.** Validation of the response output $V_{C2}$ using the pulse generator for disturbance.

Finally, the depiction of the initial disturbance variation, as described earlier using the two-step blocks, is presented.

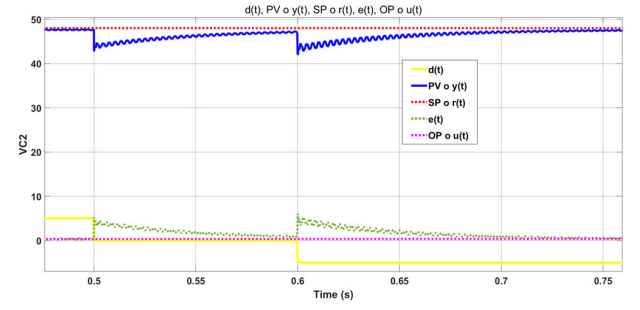


**FIGURE 11.** Closed-loop feedback employing a passivity controller.

The tables and graphs in this section are adapted from Acosta-Rodríguez et al. [43].

## IX. PID REGULATION FOR THE QBC

In line with the operational attributes of the PID regulator, it's imperative to incorporate: The controller's proportional function, Kp, aimed at shortening the rise time to maintain minimal error at a steady state. Subsequently, introduce an integral control, Ki, tasked with minimizing the steady-state error as much as possible without adversely affecting the transient performance. Lastly, a derivative control, Kd, is employed to fine-tune the transient behavior, reducing overshoot, and enhancing system stability [35].

### A. ANALYSIS OF THE ROOTS OF THE SYSTEM

For the system characterized by the transfer function outlined in equation 38, the resultant system aligns with the design parameters depicted in Figure 12, which correspond to the following:

$$\frac{2.744\text{e}10\ \text{s}\hat{}2 + 4.257\text{e}13\ \text{s} + 7.432\text{e}18}{\text{s}\hat{}4+1.228\text{e}04\text{s}\hat{}3+3.643\text{e}08\text{s}\hat{}2+1.979\text{e}12\text{s}+1.055\text{e}11}$$

The system's poles are as follows:

$$-0.3111 + 1.7801\text{i}, -0.3111 - 1.7801\text{i}, -0.6059 + 0.0000\text{i}, -0.0000 + 0.0000\text{i}$$

The system's zeros are:

$$-0.0776 + 1.6440\text{i}, -0.0776 - 1.6440\text{i}$$

Upon examining the locus of the roots, it is evident that the intersection point with the imaginary axis is determined by:

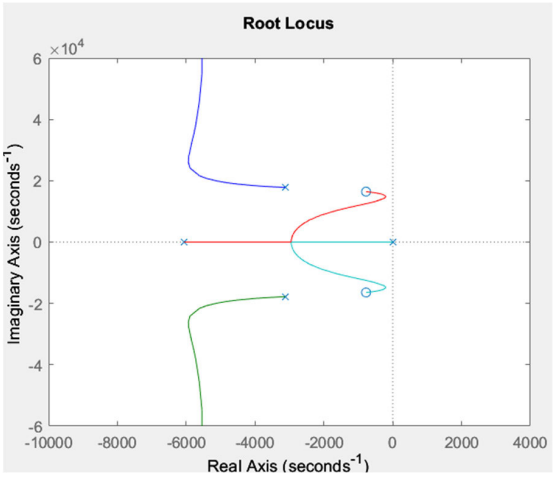


**FIGURE 12.** The system's pole and zero locations.

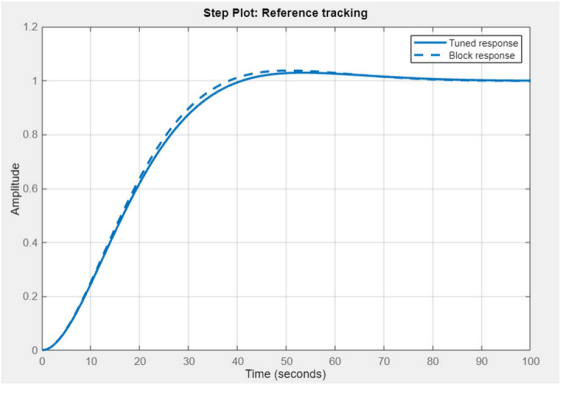


**FIGURE 13.** The system's desired output response preceding array PID.

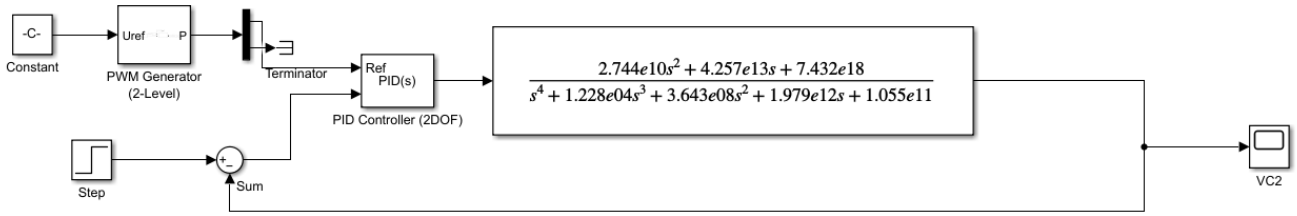


**FIGURE 14.** Implementing PID control on the plant.

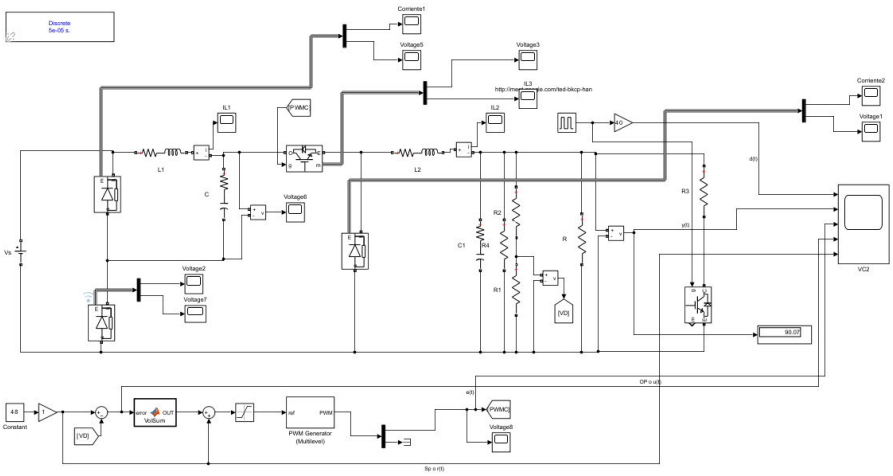

**FIGURE 15.** S-function model and circuit arrangement for fine-tuning PID response.

By examining the root locus, it becomes apparent that the system's poles fall within the range: $S = \pm j1.78$, nd the gain at the intersection with the imaginary axis is $k = 0$ and $k < 0$, The PID tuning process involves adjusting the parameters based on the desired output of the system to enhance the stability of the overall response. Furthermore, Figure 13 illustrates the tuning process, confirming the adjustment of all constants to optimize the output.

Figure 14 illustrates the PID tuning process applied to the quadratic Buck System. Adjustments in tuning involve determining the values of the system's proportional, integral, and derivative constants.

In Figure 15, a PID control algorithm is applied to achieve improved response time in the system. This algorithm is implemented through a circuit configuration designed to facilitate the desired response.

The process of the algorithm is described as such: The 'error' variable is utilized to compute the result of the 'Sumvoltage' operation, thereby regulating the QBC's output voltage. The error is calculated by taking the difference between the measured output voltage (V out) and the reference voltage (V ref). When establishing the permissible range for the 'error' variable, it's critical to consider the control's objective alongside the desired accuracy and responsiveness. For instance, to maintain the output voltage in close alignment with the reference voltage, the 'error' range might need to be confined to a narrow band (e.g., between -0.1 VDC and 0.1 VDC). Conversely, if precision and sensitivity are less critical, a broader range for the 'error' may be acceptable.

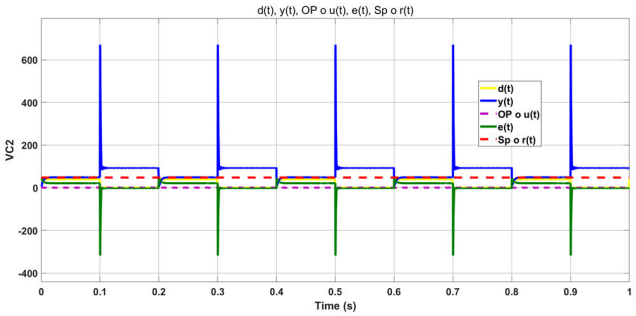


**FIGURE 16.** Output response presented in conventional formats.

To normalize the output setup, the variables are assigned based on established norms for depicting the specified parameters, as follows: The disturbance function is denoted by the yellow line d(t), derived from a square wave pulse generator with a 5 VDC amplitude, the blue line y(t) denotes the controlled variable or output of the system, which is calibrated to a 48 VDC output. The setpoint or target value is illustrated by the red signal r(t), the error signal is represented by the green line e(t), and the violet line u(t) signifies the input or control pulse signal to the system. The resultant behavior at the output is documented in Figure 16.

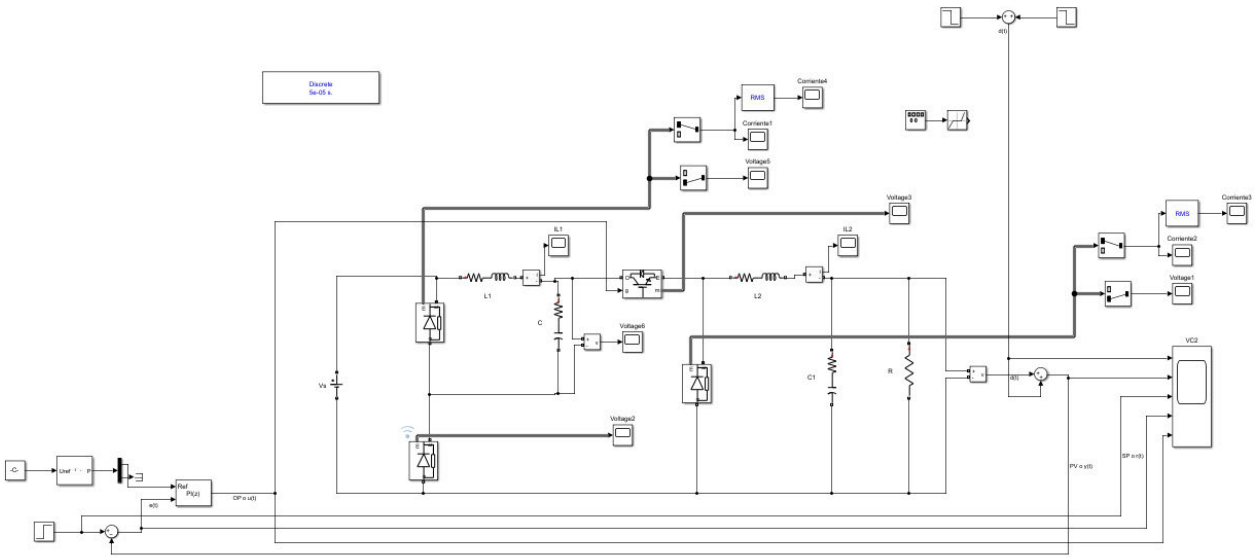

**FIGURE 17.** The circuit configuration for system response.

Nonetheless, the response typically exhibits an overshoot during disturbance rejection, which is mitigated by the subsequent circuit configuration.

Nevertheless, the reaction tends to exhibit an overshoot when rejecting the disturbance, a behavior mitigated by the subsequent circuit arrangement.

In this context, The S function is configured to function as a second-order PID controller, with response times being fine-tuned according to circuit parameters. Disturbances of amplitudes -5 and 5 were deliberately chosen for calibration, leading to the representation depicted in Figure 18. The standard system configuration is maintained to ensure ease of interpretation.

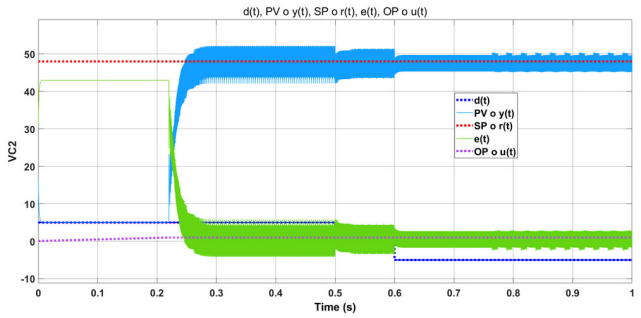


**FIGURE 18.** System response arrangement to disturbances.

A slight alteration in response to the disturbance, as depicted in FIGURE 19, notably enhances the overall system response. Considering this setup, the responses concerning $v_{C1}$, $iL_1$, $iL_2$, and $v_{C2}$ can be verified. The graphical representation of the response in $v_{C1}$ is provided below:

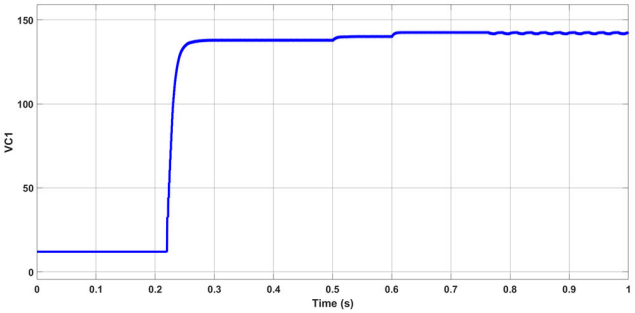


(a) The reaction of $v_{C1}$ to fluctuations in the disturbance.

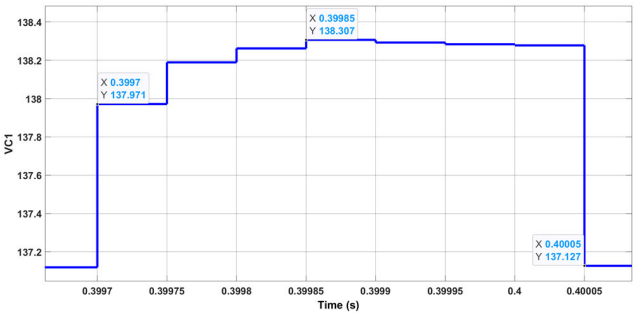


(b) Delta of the signal in a permanent mode of $v_{C1}$ in a steady-state condition.

**FIGURE 19.** The reaction of $v_{C1}$ to the PID setup.

The graph below illustrates the response of $iL_1$:

The response of $iL_2$ is depicted in the following graph:

The graph in FIGURE 23b displays the response of $vc_2$, following convention where the red line represents the reference, and the blue line represents the digital response at the capacitor's output.

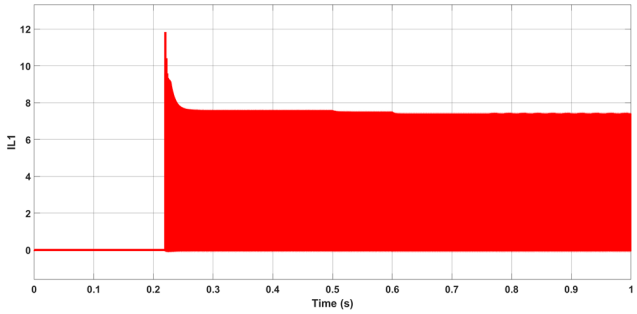


(a) The reaction of $iL_1$ to changes in the disturbance.

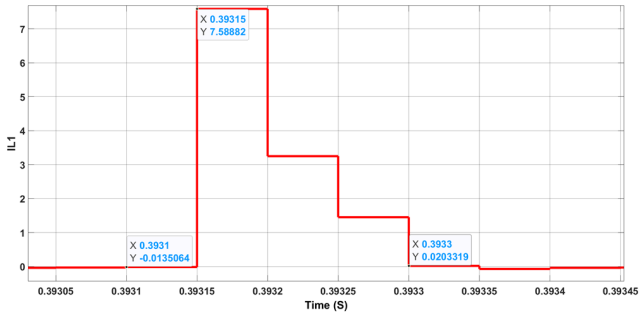


(b) The change in signal of $iL_1$ in a steady-state condition.

**FIGURE 20.** The reaction of $iL_1$ in the steady-state.

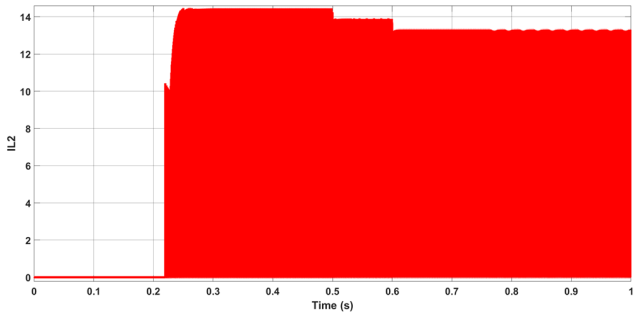


(a) The Response of $iL_2$ to Disturbance Variations.

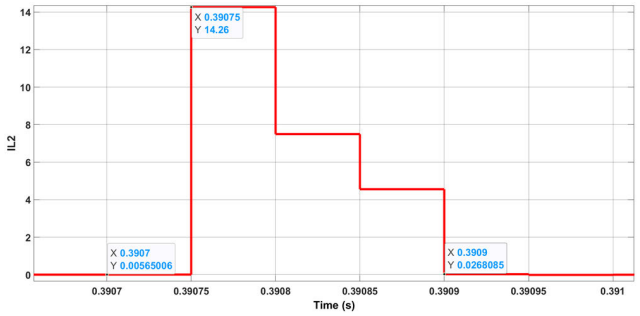


(b) he changes in the signal of $iL_2$ in a steady state condition.

**FIGURE 21.** The response of the PID array.

## X. EXPERIMENTAL PROGRESS

The development is experimental and comprises two primary phases. Firstly, it entails the meticulous design of the QBC's printed circuit, adhering meticulously to IPC manufacturing standards, thereby facilitating the realization of the actual system or plant. Concurrently, this phase also encompasses

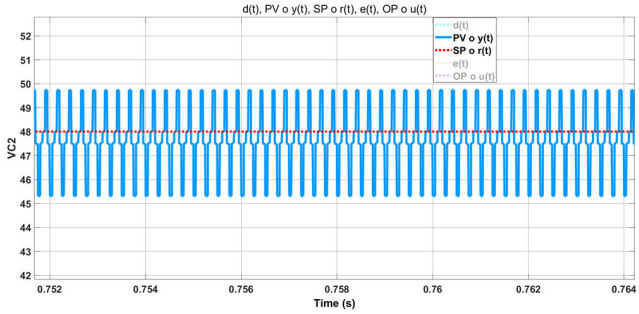


(a) The Response in Permanent Mode.

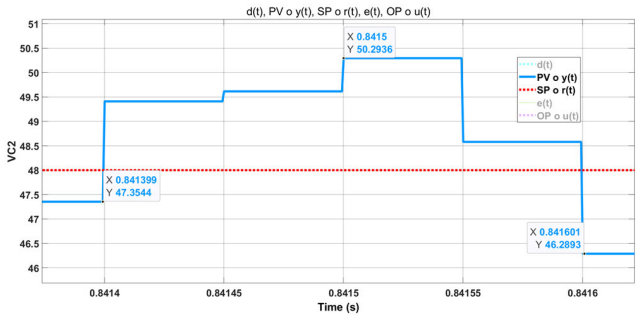


(b) The change in signal of Vc2 in a steady-state condition

**FIGURE 22.** The response of the Vc2 to the PID array.

the comprehensive validation of the three control laws expounded within this article. It is noteworthy, however, that this initial phase will not be underscored extensively at present, as the primary aim is to juxtapose the design timelines and phases pertinent to system development. Consequently, the principal objective of this research endeavor is to authenticate the efficacy of rapid prototyping design, which constitutes the subsequent phase within the experimental development [43].

### A. DESIGN OF THE PRINTED CIRCUIT

The design of the printed circuit board (PCB) strictly adheres to the IPC (Association Connecting Electronics Industries) standards, a globally recognized authority in electronics manufacturing regulations. These standards are paramount for ensuring the quality, reliability, and consistency of electronic products. Throughout the various stages of development, especially during PCB design and manufacturing, compliance with IPC standards sets rigorous benchmarks for quality assurance and performance optimization. Adhering to IPC standards is essential for enhancing the reliability and safety of the final product, particularly in terms of electronic component selection. By adhering to IPC standards, the requirements for electronic components are clearly defined, facilitating optimal component selection. Notably, the primary active components used in the PCB development include: [43].

The PCB (Printed Circuit Board) design, conversely, is performed using the ORCAD program, in compliance with IPC standards. (Association Connecting Electronics

**TABLE 5. Components employed in the design.**

| component | Characteristic | Reference |
|---|---|---|
| Diode | High-speed diodes rated at 600V and 15A | MUR1560 |
| Diode | Schottky diodes ranging from 20V to 100V | SK310A-LTP |
| power regulation | Driver stage integrated circuits converting 5V to 3.3V, with a current capacity of 1A | RFM-0505S |
| high gain, low drift instrument ation amplifier | Instrumentation amplifier offering adjustable gain from 1 to 10,000 and a bandwidth of 200 kHz | AMC1200 |
| High-speed Operationa l Amplifier | Operational amplifier with a 3GHz bandwidth and a slew rate of 7000 V/µs | THS4524_H |
| voltage converter | Converts input voltages from 9 to 36 VDC to an output of 15 VDC, supporting a maximum current of 1.2A | VQA-S9-D15-SIP1 |
| switching regulator | Regulator handling input voltages at 28V, with an output voltage range from 0.8V to 24V and a maximum current of 2.5A | TPS54286 PWP |
| Precision Adjustable Voltage Reference | Voltage reference set at 25V, operational current at 100mA. | ATL431LI BQDBZR Q1 |
| Velocity control | Control device operating between 2.7V to 5.5V, with a current rating of 50mA | TC654 |
| Hall effect current sensors | Current sensors supporting 5A, 20A, or 30A, operating voltages between 4.5V and 5.5V, with a current rating of 10mA | ACS712 |
| Semicondu ctor Power Module | Power module with a voltage rating of 600V and a current rating of 54A | IRGP4660 D |
| MOSFET semicondu ctor | MOSFET with a voltage rating of 100V and a current rating of 80A | CSD18535 KTT |

Industries) standards, which delineate the prerequisites for PCB design. These standards encompass criteria such as pin density, conductor spacing, perforation dimensions, and other pertinent specifications.

Regarding manufacturing, IPC standards dictate the requisites for PCB production, encompassing material quality, perforation tolerance, soldering quality, and additional parameters.

Tests and verification procedures are conducted under IPC standards, which stipulate the criteria for testing and verification, encompassing electrical, mechanical, and operational evaluations.

The utilization of IPC standards serves to guarantee that the design and production of electronic cards meet specified standards of quality and performance, thereby improving the dependability and safety of the product.

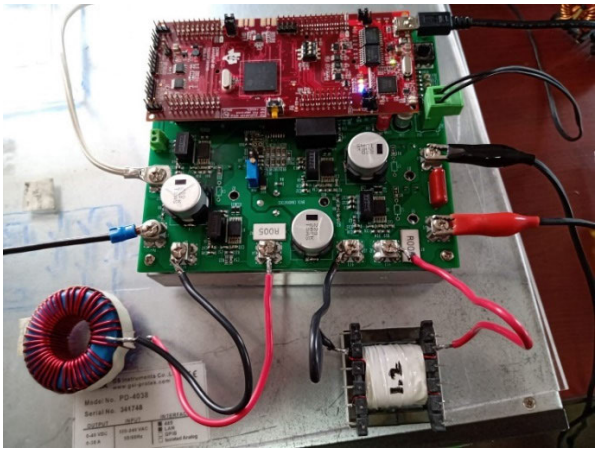

**FIGURE 23. Execution and validation of quality-based control (QBC).**

Ultimately, adhering to standard validation procedures, the control strategies undergo testing and verification using a DSP-Launchxl-f28379d, to present the results in a forthcoming publication. While these responses closely resemble the simulations, they do not achieve the same level of precision as those obtained through the rapid prototyping method discussed earlier [43].

The experiment addresses two overarching aspects. At first, the objective is to examine the timeline linked with the industrial design and implementation of an electronic card that meets applicable standards and technical requirements. This covers all stages from the initial design and simulation to assembly and testing, integrating suggested control methods like passivity-based control and PID control configuration. This methodology stands in contrast to the simulation validation conducted using the dSPACE CP1103 Control Desk, thereby curtailing expenses related to unnecessary material tests and prolonged component selection processes, which typically involve exhaustive reviews of technical data sheets potentially containing pertinent implementation details.

Furthermore, it diminishes the necessity for conducting wear tests on components, evaluating thermal dissipation, and assessing maximum voltage and current thresholds, among other considerations. The second aspect focuses on employing the implemented card for direct testing alongside the dSPACE CP1103 through rapid prototyping methods. Even though dSPACE simulation algorithms generate results that closely align with the actual system behavior, direct testing facilitates a more comprehensive validation process mirror real-world scenarios, dSPACE allows for the card's connection to DAC and ADC ports, serving as a bridge the connection between the control signal generated by PWM and the feedback of the system allows for real-time monitoring of output signals using an oscilloscope,

even though the algorithms accurately represent the actual responses.

### B. RAPID PROTOTYPING DESING

The experimental development specifically opted for the utilization of the dSPACE CP1103 tool owing to its advanced features in real-time simulation, comprehensive libraries, and seamless integration spanning from mathematical modeling to tangible hardware. In the realm of rapid prototyping, dSPACECP1103 emerged as a preferred choice due to its adeptness in handling real-time system disturbances.

dSPACE, renowned for providing an array of tools and solutions for system development, encompasses a spectrum of offerings including simulation and test systems such as MIL, HIL, and SIL, alongside automotive and process control systems. The integration platform provided by dSPACE streamlines the utilization of MIL, HIL, and SIL through rapid prototyping by enabling the simulation of complete systems at varying levels of abstraction, from mathematical models to tangible hardware. Moreover, it facilitates direct linkage between mathematical models and hardware, enabling real-time design validation. Furthermore, dSPACE offers a plethora of libraries, tools, and functionalities aimed at simplifying the simulation and testing processes, thereby reducing development time and enhancing system reliability.

The ensuing results depict the validation of rapid prototyping in real-time, showcasing the implementation of various controls such as passivity-based control (PBC) and PID arrangements, followed by the analysis of output variations concerning disturbances of 100 Hz and 500 Hz, as previously discussed (Acosta-Rodríguez, 2023) [43].

The experiment on rapid control prototyping comprises two distinct phases. Initially, simulations are conducted using the Control Desk interface, serving as the software in the loop within the dSPACE environment. This interface, akin to a desktop environment, encompasses all requisite configurations to execute simulation schemes, leveraging tools such as Simulink within MATLAB. It facilitates the observation of simulated signal behavior, duly confirmed Through the output linked to an oscilloscope using the DAC ports. The signal is sent to an oscilloscope using the DAC ports. The initial stage involves developing each control simulation, with the primary PCB control board being the focal point of the simulation and embedded system, as illustrated in figures 27 and 28, utilizing dual-loop feedback (C3) and digital output.

Following this, we introduce two distinct types of perturbations, each occurring at frequencies of 100 Hz and 500 Hz, as visually depicted in Figures 30 and 31. The aim is to assess the impact of power supply disturbances, arising from fluctuations in voltage or inherent noise within the power supply, these disturbances can impact the operational effectiveness of the circuit. Such disruptions might originate from the electrical grid or other interconnected devices drawing power from the same source.

In industrial or high-power equipment environments, there exists a susceptibility to Electromagnetic Interference (EMI), notably through wiring from the power source. A second type of disturbance, occurring at 100Hz, pertains to factors influencing output load stability and reliability. These factors include Load Noise,

In scenarios where the attached load has the potential to cause output variations, particularly crucial in fields like audio technology or telecommunications, the circuit's output impedance becomes pivotal in facilitating energy transfer to the load. This underscores the significance of suitable impedance alignment. Verification of filters and regulators in the input/output circuit can mitigate circuit noise, ensuring stable output despite input variations. Addressing cable types and quality in simulations ensures robust connections, minimizing circuit-related issues. Protection becomes a crucial factor in environments susceptible to electromagnetic interference, as employing targeted shielding in particular circuit segments can offer substantial advantages in minimizing noise and preserving signal integrity [43].

Crucial considerations must be considered for the accurate fabrication of the switch by the manufacturer. Utilizing the Control Desk, simulated tests were conducted to evaluate the PID array control, as depicted in Figure 32. Throughout these assessments, adjustments were made to the algorithm to extract specific data from the system's dual-loop feedback outputs, as demonstrated in Figure 33.

To gauge the robustness of the control system against external factors, system disturbances were introduced based on Figure 34. One disturbance, occurring at a frequency of 100Hz, aimed to assess the system's response to voltage fluctuations or power supply noise in the input environment. Another disturbance, operating at 500 Hz according to Figure 35, Focused on intermediary levels and output disruptions like load disturbances, output impedance, validation of filters and regulators, cable integrity, and the efficiency of shielding. These simulations were conducted to replicate real-world conditions and evaluate the system's performance comprehensively.

The subsequent part entails seamlessly incorporating the implemented card with the dSPACE CP1103, thereby establishing a connection between the output of the control simulator and the input signal of the IRGP4660D-EPBF, with the output directly linked to the oscilloscope. Significant testing variations involve 500Hz input disruptions, which are frequently encountered in settings characterized by audio, communication, and susceptibility to interference. Similarly, real-world conditions impact 100Hz disturbances that affect the output [43].

In the next step, assessments for both control techniques are confirmed. Concerning the approach based on passivity, a specially designed rectangular or square component is employed for two signals that are directed into the input of the IRGP4660D-EPBF switch. One signal imposes a maximum resistance of 5.1 ohms, while the other imposes a minimum resistance of 3.3 ohms. As illustrated in Figures 24a and 24b,

the Control Desk simulation incorporates a self-identifying (SIL) program algorithm, enabling automatic adjustments in the duty cycle percentage. This leads to an observed output signal of 48.11VDC on the oscilloscope.

Finally, the output is measured to the PID array control represented in Figure 25, the duty cycle gradually adjusts in response to changes in resistance, specifically 3.3, 4.7, and 5.1 ohms. This adjustment is verified by the Safety Integrity Level (SIL) within the algorithm overseeing the simulation effects in the Control Desk. Consequently, the output measures 48.3 VDC, closely aligning with the simulated value.

This research builds upon prior seminal works and combines advanced methods referenced in [40], [41], and [42] to tackle harmonic distortions and 'chattering'. Utilizing fractional and adaptive approaches, it effectively suppresses harmonics and enhances active power filter performance, as demonstrated through experiments. Furthermore, experimental validation of these strategies, including passivity-based control and sliding mode control, is showcased in [8] and [43], employing real-time rapid prototyping techniques. Notably, the articles [5], [7], [9], [10], [12], [13], [14], [15], [21], [25], and [26], present a variety of technics in control strategies to enhance the stability and performance of electrical systems, especially in the context of distributed generation and power converters. Advanced control methods are proposed, such as passive control based on passivity and nonlinear fuzzy control, and sliding mode, to address specific challenges such as voltage ripples, current harmonics, and instability in DC. Additionally, hybrid approaches combining multiple control techniques, such as proportional-resonant control and fractional-order sliding mode control, are explored to improve system dynamic response and robustness [40], [42]. Passivity-based co-design methods are highlighted to ensure the stability and compliance of devices under test [33], [43], as well as data-driven and frequency-domain control approaches to mitigate high-current oscillations in [13], [21], and [25]. Simulation and hardware experiment results validate the effectiveness of these control approaches in a variety of practical applications, demonstrating their potential to enhance the efficiency and reliability of electrical systems overall [11], [12], [18], [19], [26]. This study contributes valuable insights applicable across a spectrum of applications within the field.

### C. QBC UNDER DIFERENT LOADS

Given that the actual results closely resemble the experimental results obtained during testing the two controls on the dSPACE 1103 rapid prototyping is conducted to ensure that load changes are validated with either control, preventing any bias from robust control. To reduce noise in the output voltage, either a 500 W or minimize interference in the output voltage, the card or system includes either a 500 W power circuit or a low-pass filter with a frequency of 100 kHz. For the load change test involving the PI type II controller, an ISO5452-Q1 driver is utilized, set up with a 100 ms time constant, and powered by a 15 VDC floating power supply to enable the operation of the integrated circuit.

In Figure 24, the real load variation of 4.98A is depicted under the application of Passivity-based control using resistors with values of 3.3 ohms, 4.7 ohms, and 5.1 ohms. This setup is engineered to achieve a targeted output voltage of 48.1 VDC.

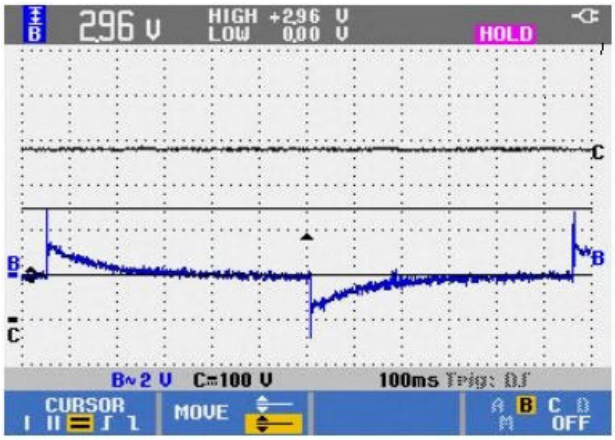


(a) Development of a closed-loop oscilloscope output printed circuit board (PCB) optimized to maintain peak performance under load variations.

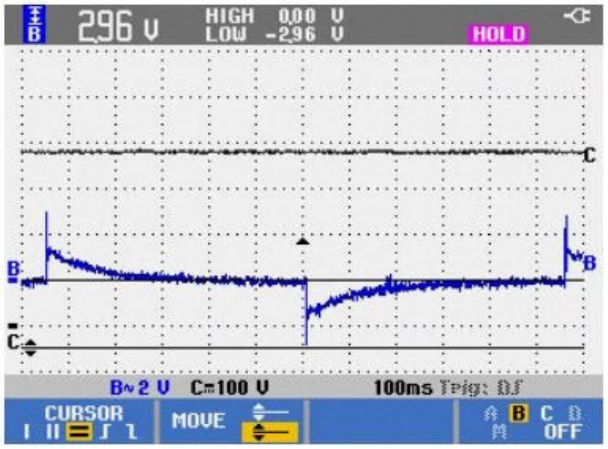


(b) Design and implementation of a closed-loop oscilloscope output printed circuit board (PCB) engineered for minimal deviation during load variations.

**FIGURE 24. (PCB) for oscilloscope output, ensuring optimal performance across both maximum and minimum load variations.**

The results confirm the controller's precise performance and confirm the suggested solution detailed in the project. To detect voltage surges when the load changes, the oscilloscope settings are tweaked to reduce the DC part of the signal and record the peak voltage variation. When the load changes in real-time, the inverter maintains a constant voltage level of 48.1 VDC.

In FIGURE 25, a regulated electrical output of 48.3 VDC is depicted, accompanied by a recovery time of 10ms,

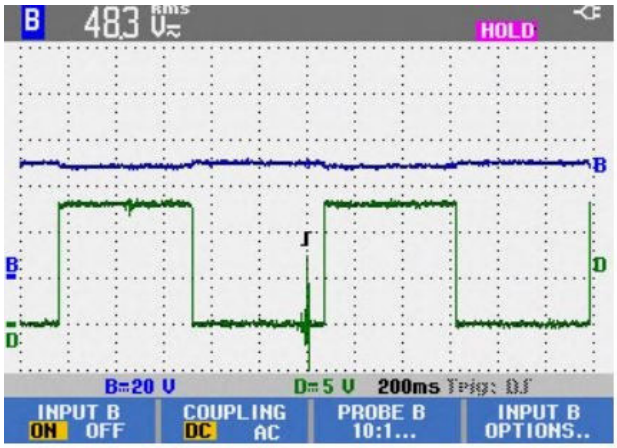


**FIGURE 25.** Engineering and testing of a PID array-based oscilloscope output module operating with a 380 VDC input power source.

as evidenced in the same figure. Additionally, the converter exhibits a recovery time of approximately 10ms under load conditions with a voltage variation of 48.3 VDC.

These results confirm the precise implementation of the controller and verify the proposed solution described in the project.

The change in actual load, recorded at 4.98A, is noticeable when using the PID array control with resistors of 3.3 ohms, 4.7 ohms, and 5.1 ohms. This configuration is designed to achieve a targeted response in the output voltage of 48.3 VDC.

The oscilloscope outputs, depicted in FIGURE 24 and FIGURE 25, serve to validate the successful implementation of the controller. The regulated electrical output of 48.1VDC, accompanied by a rapid recovery time of 10ms across various load conditions, underscores the robustness and reliability of the system. These empirical findings strengthen the theoretical foundations laid out, confirming the project's efficacy in enhancing power system quality and stability.

The tables and graphs in this section are adapted from Acosta-Rodríguez et al. [43].

These visual elements are included here to provide relevant context and have been modified solely to meet the needs of the current study. For graphs, similar adaptations were made with distinct data points, representing the current study's findings.

## XI. ANALYSIS OF RESULTS

Here is a tabulated summary detailing the outcomes concerning the parameters for each control methodology.

Based on the preceding Table 6, the values of the controls that closely resemble the theoretically derived references exhibit variability. For instance, considering the $\boldsymbol{vc_1}$ with a reference of '135.0555', the PID array achieves '137.971'. This attainment is promptly reached at '0.3997' s. However, it slightly surpasses the anticipated range, peaking at '138.307' within '0.40005' s, albeit insignificantly. Notably,

**TABLE 6.** Parameter values for each controller.

| PERFORMANCE INDEX | | | | | | |
|---|---|---|---|---|---|---|
| Controller measurement | | | | | | |
| Passivity | | | | | | |
| | min | max | dif | t_min | t_max | dif |
| vc1 | 133,817 | 133,957 | 1,40E-01 | 0,497003 | 0,499706 | 2,70E-03 |
| il1 | 3,55878 | 3,61656 | 5,78E-02 | 0,296368 | 0,299328 | 2,96E-03 |
| il2 | 10,2477 | 10,263 | 1,53E-02 | 0,496613 | 0,499553 | 2,94E-03 |
| vc2 | 48,0842 | 48,1195 | 3,53E-02 | 0,395668 | 0,398686 | 3,02E-03 |
| PID | | | | | | |
| | min | max | dif | t_min | t_max | dif |
| vc1 | 137,971 | 138,307 | 3,36E-01 | 0,3997 | 0,40005 | 3,50E-04 |
| il1 | -0,0135064 | 7,58882 | 7,60E+00 | 0,3931 | 0,3933 | 2,00E-04 |
| il2 | 0,00565006 | 14,26 | 1,43E+01 | 0,3907 | 0,3909 | 2,00E-04 |
| vc2 | 47,3544 | 50,2936 | 2,94E+00 | 0,841399 | 0,841601 | 2,02E-04 |

the $\boldsymbol{iL_1}$ currents fluctuate from '-0.0135064' to '7.58882', while $\boldsymbol{iL_2}$ ranges from '0.00565006' to '14.26'.

In the scenario involving $\boldsymbol{iL_1}$ under the passivity-based control PBC, the initiation occurs slightly earlier at '3.55878' for '0.296368', with minimal disparity observed in short timeframes estimated by both controls, ultimately reaching '3.61656' within '0.299328' s.

Regarding $\boldsymbol{iL_2}$ with a reference of '10.4167', the passivity-based control PBC demonstrates swifter convergence to a close value, achieving '10.2477' in only '0.496613' s, yet it subsequently attains '10.263' in '0.499553' s.

Lastly, in the context of the output Vc2 with a reference of '48', the passivity-based control PBC achieves a more precise approximation, initiating with a very close value of '48.0842' within '0.395668' s and subsequently reaching '48.1195' within '0.398686' s. Conversely, the PID arrangement attains a peak of '47.3544' at '0.841399' s and later reaches '50.2936' with a delay of '0.841601' s.

In this context, $\boldsymbol{vc_1}$ denotes the control voltage, while $\boldsymbol{iL_1}$ and $\boldsymbol{iL_2}$ represent distinct current parameters.

### A. PERFORMANCE INDEX

Control performance indices serve as metrics for evaluating the effectiveness of a control system within each process. These indices enable comparisons between various control systems and gauge the extent to which a control system achieves its predefined objectives. Key metrics include response time, precision, stability, and resilience [36].

### B. PERFORMANCE INDICES

Various metrics can assess control process effectiveness, including the Performance Index (PI), Capability Index (Cp), Enhanced Capability Index (Cpk), and Z-Performance Index (Z-score) undergo assessment. The Performance Index (PI) evaluates process quality by comparing the desired characteristics and current values, which are divided by the desired value [37]. The Capability Index (Cp) measures adherence to tolerance specifications by comparing tolerance limits to twice the process standard deviation. The Enhanced Capability Index (Cpk) indicates consistent adherence to tolerance and is the lower of Cp and the quality capability index (Cpk = min (Cp, CPU)).

The Z-performance index (Z-score) quantifies the extent of deviation of a specific value from the anticipated value, determined by comparing the expected value with the current

value, divided by the standard deviation of the process [38]. The primary indices, such as PI, Cp, Cpk, and Z-score, are summarized in Table 7.

**TABLE 7.** Performance indices such as PI, Cp, CpK, and Z-score.

| Experimental performance index | | | | |
|---|---|---|---|---|
| Passivity | | | | |
| | PI | Cp | Cpu | Z score |
| vc1 | 1,04E-03 | 4,091489918 | 4,188411845 | 0,528913683 |
| il1 | 1,56E-02 | 0,020492319 | 0,023344054 | 0,041234563 |
| il2 | 0,001468795 | 0,095134876 | 0,096749962 | 0,001208048 |
| vc2 | 7,35E-04 | 0,021837896 | 0,023628221 | -0,78539784 |
| PID | | | | |
| | PI | Cp | Cpu | Z score |
| vc1 | 2,49E-03 | -0,005335307 | 0,037654218 | -8,47108677 |
| il1 | 2,05E+00 | -4,351957486 | 2,430040981 | -1,4522442 |
| il2 | 1,37E+00 | -14,04438009 | 10,4243232 | -0,7463104 |
| vc2 | 6,12E-02 | -0,644877021 | 0,440553699 | -2,07025316 |

A PI above 1 indicates the process operates above the desired value, while a PI below 1 suggests operation below the desired value. A PI close to 0 indicates proximity to the desired value. Keeping this principle in mind, several values are extremely close to zero across all three controls. For example, regarding $v_{C1}$, it can be observed that it approaches zero in all controls. However, it is closest to zero with the passivity-based control PBC, at '1.04e-03' followed by the PID array at '2.49e-9'. Concerning $iL_1$, the smallest value is seen in the passive control at '1.56e-02' followed by the PID array at '2.05e-00'.

For $iL_2$, the passivity-based control PBC demonstrates the closest approximation to zero with '0.001468795', followed by the PID array with '1.37'. In the case of Vc2, the passivity-based control PBC exhibits the lowest value '7.35e-04', followed by the PID array at '6.12e-02'.

A CPU value above 1 indicates enough processing capacity to meet tolerance requirements, whereas a value below 1 suggests insufficient. While the values in Table 7 are close to 1, notable observations include those of the PID array, with $iL_1$ of '2.4300400981' and $iL_2$ '10.4243232'.

A high Z-score indicates a value significantly exceeding the expected value, while a low Z-score suggests the opposite. That the value falls notably below the expected value. Notably, in the case of the passivity-based control PBC, the Z-scores are noteworthy. For $v_{C1}$ it records '0.52891368', for $iL_1$ it is '0.04123456', and the lowest among them is for $iL_2$ with '0.00120805', albeit this value is relatively inconsequential. Conversely, unfortunately, in the PID array, the values of the variables are very small.

### C. PERFORMANCE INDICES (ISE, ITSE, IAE, ITAE)

Here are the key findings concerning the analysis of performance index behavior, based on those commonly used in industrial settings.

The ITAE metric is selected based on its utility in evaluating process control system performance. It measures the integral of time-weighted absolute error, indicating how promptly errors are corrected and system stability. In switching converters, ITAE is crucial for assessing controller performance regarding stability attainment and system distortion levels. Utilizing ITAE enables controller designers to enhance system stability and minimize distortion, thereby improving system quality and reliability.

### D. INTEGRAL OF TIME MULTIPLIED BY ABSOLUTE ERROR CRITERION (ITAE)

The Multiplied Time Integral Absolute Error (ITAE) criterion is a quantitative measure used in process control methods to assess the temporal variation of a process. It involves integrating the absolute difference between the desired and measured process values over time, thereby encapsulating both the amplitude and duration of deviations from the desired state. This criterion is particularly pertinent in Control by Attribute (CA) analyses, where it aids in assessing the efficacy and performance of the controlled process. Mathematically, the ITAE is expressed as the integral over time of the absolute deviation between each process measurement and the desired setpoint, represented by the formula: ITAE ITAE $= \int$ t |xi – x_wanted | dt [39].

In this equation, 't' signifies the elapsed time since the initiation of a process alteration, 'xi' represents each discrete process measurement, and ''x_wanted'' represents the desired target value for the process, under consideration.

**TABLE 8.** ITAE performance indexes.

| ITAE INDEX | |
|---|---|
| Passivity | |
| ITAE | |
| vc1 | 1,93E-01 |
| il1 | 1,65E-02 |
| il2 | 3,15E-02 |
| vc2 | 1,05E-02 |
| PID | |
| ITAE | |
| vc1 | 1,04E-02 |
| il1 | 2,33E-03 |
| il2 | 2,33E-03 |
| vc2 | 4,50E-03 |

A diminutive value of the Multiplied Time Integral Absolute Error (ITAE) criterion signifies a process characterized by stability and minimal temporal variability. This metric serves to gauge the dynamic behavior of a process over time, with lower ITAE values indicative of enhanced process performance. However, it's imperative to acknowledge that while ITAE offers valuable insights into process stability, it should be complemented with additional evaluation criteria to attain a comprehensive assessment of process performance. As delineated in Table 8, most variables across all control configurations exhibit stable behavior. Notably, for v_C1, the PID array demonstrates an ITAE value of '1.04e-02',

followed by the passivity-based control with '1.93e-01'. Likewise, for $iL_1$ the PID array yields '2.33e-03', while the passivity-based control records '1.65e-02'. The trend continues for $iL_2$ with the PID array registering '2.33e-03' compared to the passive control's '3.15e-02'. Finally, for the Vc2 output, the PID array exhibits '4.50e-03', trailed by the passivity-based control at '1.05e-02'.

### E. GENERAL CONSIDERATIONS

The passivity model exhibits a dynamic response characterized by rapid stabilization, achieving stability within approximately 0.3 s. Tests conducted with disturbances ranging from -5VDC to 5VDC, each lasting 0.5 to 0.6 s, reveal a swift recovery of nearly 0.1 s following each disturbance. This behavior is depicted in FIGURE 26, illustrating the model's robustness against disturbances, a characteristic shared with other robust control strategies, as demonstrated in Figure 10. Conversely, when subjected to a sequence of 5VDC pulses, the system exhibits sensitivity to disturbances, stabilizing the signal in approximately 0.1 s. The signal ripple, ranging between 48.0842 and 48.1195, closely approaches the reference value within 3.018 ms. At the experimental level, perturbations at frequencies of 100Hz and 500Hz are introduced using the dp1103 control desk tool, as depicted in FIGURES 30 and 31, respectively. These experiments underscore the passivity control's robustness, particularly its responsiveness to disturbances at high frequencies.

Initially, the plant's PID stability is adjusted directly, but when encountering an overdamped response, the time values are around 80 s, which is excessively large. To reduce the settling time, an algorithm is created using a MATLAB function, which digitally modifies the output value to match the reference value by adjusting the error parameters every 0.1 s. As a result, settling times occur within 0.3 s in continuous conduction mode, but take up to 0.8 s in steady-state mode to achieve the desired value, as shown in FIGURE 22. The accuracy of the output voltage ranges between 47.3544 VDC and 50.2930 VDC for durations of 202 $\mu$s, as shown in FIGURE 19. It's worth noting that this PID arrangement strategy enhances its response speed by nearly 0.8 s.

The responsiveness of this configuration is comparatively slower than that of other controls, with its response to the disturbance causing a peak of 10 volts above the reference at 0.6 s, followed by automatic rectification to achieve steady-state mode, as shown in FIGURE 16.

The sensitivity is improved with the integration of the algorithm function, as its behavior previously exhibited numerous excessively high peaks when confronted with a specific disturbance in a square wave sequence, as demonstrated in Figure 16.

The experimental response is validated by introducing disturbances of 100Hz and 500Hz, confirming the actual dynamics observed in the simulation conducted using the Control Desk tool shown in FIGURE 33, 34, and 35, as well as its implementation via HIL using the dSPACE CP1103. This behavior elucidates the sensitivity to disturbances of the PID control discussed earlier.

Passivity-based control is known for its ability to ensure system passivity and achieve precise reference tracking. Although it offers these advantages, it may be prone to vibration problems, such as quick oscillations in the control signal to achieve optimal performance, precise tuning of controller parameters is often required, as shown in FIGURE 24.

On the other hand, the PID array (Proportional-Integral-Derivative) of the controller is known for its stability and resilience, particularly in specific situations. Nonetheless, its effectiveness can be impacted by the selection of controller parameters and the precision of system modeling as evidenced in FIGURE 25.

In conclusion, both the passivity-based control and the PID arrangement exhibited commendable performance. Passivity-based control, however, stood out for its precision and quick stabilization. However, we observed that passivity-based control stood out for its ability to ensure system passivity and achieve particularly precise reference tracking. While the PID arrangement also exhibited stability and robustness, passivity-based control provided higher precision in our experiments, as evidenced in FIGURE 24.

There the adoption of a diverse array of control performance metrics, including the PI index, CP index, CPK index, and Z-score, is pivotal for several cogent reasons. Firstly, this multifaceted approach engenders a nuanced evaluation of control system efficacy. By amalgamating disparate performance indicators, comprehensive scrutiny ensues, elucidating latent anomalies that might evade detection when reliant solely on singular metrics.

Moreover, the utilization of multiple performance indices facilitates precise anomaly localization within the control architecture. This enables a granular diagnosis of underlying challenges, thereby enabling targeted interventions to rectify performance aberrations efficaciously.

Furthermore, the deployment of varied performance benchmarks enables comparative assessments across diverse control systems. Through the standardized application of metrics, it becomes feasible to discern optimal strategies tailored to specific applications or operational contexts.

In essence, the systematic incorporation of a diverse spectrum of performance indices confers substantive benefits in enhancing the overall efficiency and productivity of control systems. By identifying and addressing discrepancies, iterative improvements can be effectuated to optimize system performance, ultimately fostering heightened operational efficiency and productivity.

The tables in this section are adapted from Acosta-Rodríguez et al. [43], with modifications made to the values.

## XII. CONCLUSION

This study emphasizes the importance and significant benefits of employing advanced methods such as rapid

prototyping and specific control strategies in the development and implementation of electronic control systems. The findings and analyses presented throughout various sections of this document contribute to a robust understanding and evaluation of the employed strategies and technologies, as well as their impact on the development and performance of the Quad Boost Converter (QBC) and its controls.

Rapid Prototyping and dSPACE:

Rapid prototyping with dSPACE CP1103 significantly expedited design validation, offering real-time insights into system behavior and disturbances. This approach reduced development time to about a week, ensuring QBC reliability and project success.

Evaluation of Control Strategies:

Passivity-based control (PBC) demonstrated superior accuracy and rapid stabilization compared to Proportional-Integral-Derivative (PID) control. PBC excelled in achieving closer values to desired references in shorter time intervals, particularly in output voltage and currents. While PID showed robustness and stability, PBC's enhanced performance supports its preference for applications requiring precision and rapid response. The importance of using multiple performance indices for a comprehensive evaluation of the control system was emphasized.

The process of identifying parameters for the passivity-based controller entails examining stability through the application of the Lasalle asymmetric stability theorem. This theorem delineates conditions under which the system achieves stability converges to a fixed set, regardless of its initial conditions, attracting all system trajectories. As elucidated in Section VII-D, passivity control employs passivity as opposed to state feedback, ensuring that the system consumes no Increasing the system's stability and performance is achieved by extracting more energy than what is initially supplied. Employing canonical forms in conjunction with passivity control entails representing the system in a particular structure, streamlining the analysis and design process of the controller. Canonical forms, like the controllable canonical form and observer canonical form, are utilized for this purpose to provide standardized representations of the system that aid in comprehending the properties and structure of the controller, as elaborated in Sections VIII-A Controller design and VIII B Closs loop controller design. Finally, like in slider mode control, the system integrates an inner loop regulated through passivity-based control and an outer loop employing a proportional-integral (PI) controller, depicted in Figure 26 and for values of kp and ki shown in Table 9 correspondingly.

Regarding the PID controller, it is determined in section IX-A, with its transfer function derived from equation 38. The system roots, validated to ensure system stability, are verified through the graphical representation of poles and zeros in Figure 12 and the response in Figure 13. This is carried out using the block diagram presented in Figure 14. The resulting controller values are described in Table 9. However, a significant delay of 80 s is observed.

**TABLE 9. Control parameters (Kp, Ki, Kd) across various methods and algorithms.**

| | PBC | |
|---|---|---|
| Kp | Ki | Kd |
| 0.001256 | 0.100933 | 0 |
| | PID | |
| Kp | Ki | Kd |
| 7.652675e-08 | 9.062444e-09 | 3.835748e-08 |
| | ALGORITHM | |
| Kp | Ki | Kd |
| 0.0012556 | 0.1009328 | 0 |

When implementing the algorithm, following Figure 15, the signal response decreases drastically, as validated in Figure 18, for the parameters Kp, Ki, and Kd, shown below in Table 9.

Project Implementation:

The real-world implementation of the QBC took about six months, involving careful selection and programming of electronic components following IPC standards for reliability and quality assurance. Despite the lengthy development period, efficient prototyping and validation phases highlighted the effectiveness of integrating advanced tools and strategies in the process.

Performance Indices:

Performance evaluation utilized various indices such as ITAE to analyze control behavior comprehensively. Both PID array and PBC showed stable behavior across different variables, confirming robust control strategies in the QBC. Real-time experimentation integrated seamlessly with preliminary simulations conducted in Control Desk, emulating physical plant intricacies through dSPACE interface. Output relayed to oscilloscope, transduced to software for feedback analysis, ensuring consistency between current, voltage, and system response times for fidelity between simulated and real-world outcomes.

During both experimental and simulation phases, the comparison between the proposed methodology and alternative methods is aimed at confirming its effectiveness. Through this comparative evaluation, enhancements in operational effectiveness, system stability, and disturbance resistance are expected. This serves as robust validation of the appropriateness and benefits of the proposed approach over thoroughly examined alternatives. Advanced metrics such as PI, Cp, CpK, Z-score, and ITAE were utilized for comprehensive performance evaluation. These metrics assess critical aspects including response time, signal precision, system stability, and resource utilization efficiency. By incorporating these metrics, a thorough understanding of the system's performance characteristics was achieved, facilitating a comprehensive comparison with alternative methods, and effectively demonstrating the efficacy and enhancements provided by our proposed methodology.

Implications and Future Work:

This methodology is open for evaluation under alternative control paradigms, including robust controls or classical control strategies. Additionally, validation across diverse industrial plants can substantiate its efficacy under varied voltage conditions, covering a spectrum of high-performance scenarios.

The insights from this study hold substantial implications for the design and development of electronic control systems, particularly those utilizing rapid prototyping and advanced control strategies. The evident superiority of passivity-based control in ensuring precision and rapid system response underscores its potential as a preferred control strategy for similar electronic systems. Future work may delve deeper into optimizing PBC parameters for enhanced performance and exploring additional rapid prototyping tools and strategies to further streamline the development process and enhance the quality and reliability of electronic control systems.

## APPENDIX A
## CALCULATIONS TO OBTAIN VALUES

This assignment aims to confirm the calculations performed in the previous section and to evaluate the precision of these computations through simulations. It's essential to verify the capacitances, inductances, voltage, and current values under steady-state conditions, utilizing the provided dataset:

**TABLE 10.** Key parameters for PCB.

| $V_g$ | $V_0$ | $P_0$ | $F_S$ | $\frac{\Delta I_{L1}}{I_{L1}}$ | $\frac{\Delta I_{L2}}{I_{L2}}$ | $\frac{\Delta V_{C1}}{V_{C1}}$ |
|---|---|---|---|---|---|---|
| $380V$ | $48V$ | $500W$ | $100KHz$ | 15% | 10% | 0,5% |

**TABLE 11.** Parameter determination for the QBC.

| $\frac{\Delta V_{C1}}{V_{C1}}$ | D | Dp | R |
|---|---|---|---|
| $\frac{\Delta V_{C2}}{V_{C2}}$ | sqrt (Vc2/Vg) | 1-D | Vc2^2/Po |
| 0,5% | 0.3554 | 0.6446 | 4.608 |

Initially, the determination of the output resistance entails meticulous calculation:

$$R = \frac{V_{c2}^2}{P_0} = 4.6080\Omega \tag{A1}$$

Next, the derivation of steady-state values ensues by equation (39), thereby computing $\boldsymbol{I_{L2}}$

$$I_{L2} = \frac{V_{c2}}{R} = 10.4167\ \text{A} \tag{A2}$$

Utilizing equation (34), determine the value of $I_{L1}$, preceded by the calculation of the value through equation (50).

$$D = \sqrt{\frac{48}{380}} = 0.3554 \tag{A3}$$

Consequently,

$$I_{L1} = 10.4167 * 0.3554 = 3.7022\,A \tag{A4}$$

Subsequently, we proceed to determine the values for $V_{C1}$ and $V_{C2}$, using equations (30) and (32), respectively, considering the following:

$$V_{C2} = V_0 \tag{A5}$$

As a result:

$$V_{C1} = \frac{48V}{0.3554} = 135.0555V$$

Subsequently, the inductance and capacitance values are derived from the steady-state values obtained. Beginning with the calculation of inductance $L_2$ using equation (43):

$$L_2 = \frac{0.3554 * 135.0555V * (1 - 0.3554)}{2 * 100KHZ * 3.7022 * 0.10} = 4.1787e - 04H \simeq 0.4mH$$

for $L_1$ its value is determined using equation (41):

$$L_1 = \frac{0.3554 * 380V * (1 - 0.3554)}{2 * 100KHZ * 10.4167 * 0.15} = 0.2786\ H \simeq 278.6mH$$

The determination of the capacitance values culminates in the analysis, whereby the value of $C_1$ is established through equation (46), elucidating the equivalence between $C_1$ *and* $C_2$.

$$C_1 = \frac{-0.3554 * 10.4167 * (0.3554 - 1)}{2 * 100KHZ * 135.0555 * 0.005} = -1.7670e - 05F \simeq 177\mu F$$

When after determining the calculated variables, a MATLAB simulation is performed using the quadratic Buck converter block, which includes the system's transfer function. The transfer function is defined using the primary parameters outlined in Table 10 and Table 11. The voltage output spans from 135.695 to 134.342. Upon calculating the delta value, we derive:

$$\Delta_{VC1} = \frac{135.695\text{V} - 134.342\text{V}}{2 * 135.0555V} * 100 = 0.5009\%$$

In this instance, the determined delta is:

$$\Delta_{IL1} = \frac{4.729\text{A} - 2.668\text{A}}{2 * 3.7022\,A} * 100 = 27.8348\%$$

$$\Delta_{VC2} = \frac{48.017\text{V} - 47.937\text{V}}{2 * 48V} * 100 = 0.0833\%$$

$$\Delta_{IL2} = \frac{10.957\text{A} - 9.882\text{A}}{2 * 10.4167\ \text{A}} * 100 = 0.0521\%$$

Regarding the coils, the error is negligible, posing no issues for construction; in fact, it may lead to an improved response.

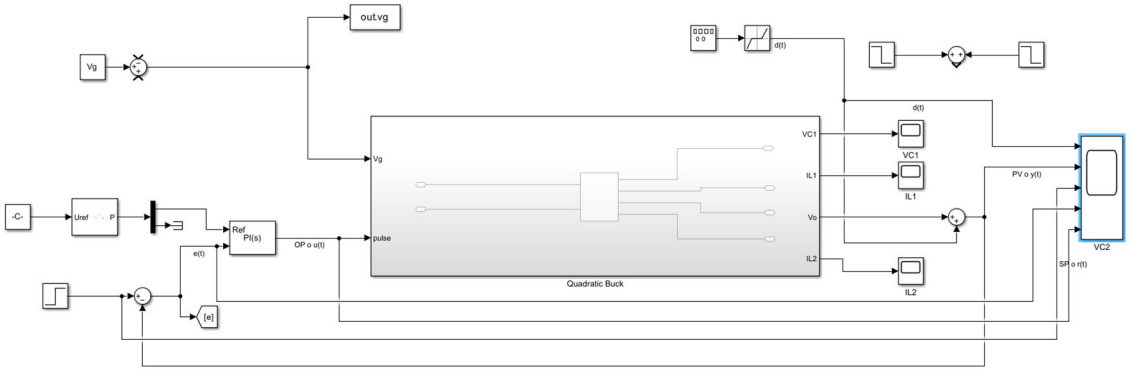


**FIGURE 26.** A block diagram illustrating the passivity-based control model.

## APPENDIX B
## QBC PCB PASSIVITY-BASED CONTROL CLOSED-LOOP CONTROLLER DESIGN

See Fig. 26.

## APPENDIX C
## EXPERIMENTAL CONTROL BY PASSIVITY-BASED CONTROL PBC

Regarding the design of the passive controller, the simulation arrangement is depicted in FIGURE 27, the passive signal arrangement is illustrated in FIGURE 28, and the dual-loop signal disruption is shown in FIGURE 29.

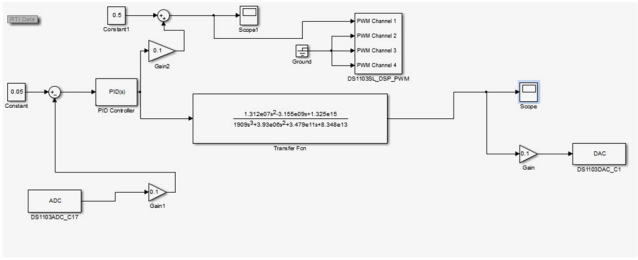


**FIGURE 27.** Establishment of passivity-based control (PBC) configuration employing a dual supply loop.

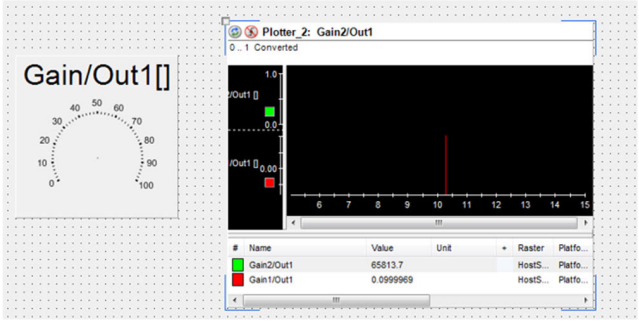


**FIGURE 28.** Analysis of signal behavior under passive-based control, with subsequent validation using an oscilloscope.

The response of the dual signal is depicted within the simulation.

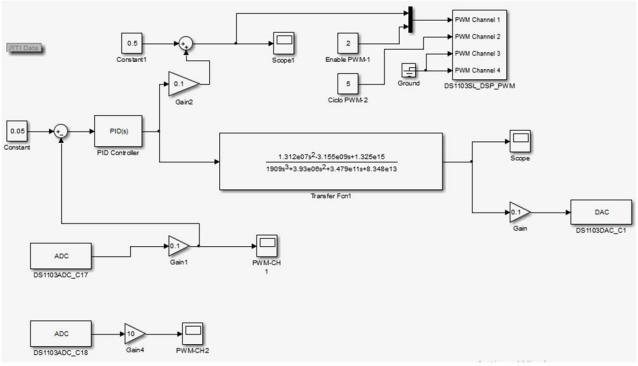


**FIGURE 29.** Dual signal output subject to disturbances.

Following that, the configuration is executed in the Control Desk for the dual-signal setup with a 100Hz disturbance, as depicted in Figure 30.

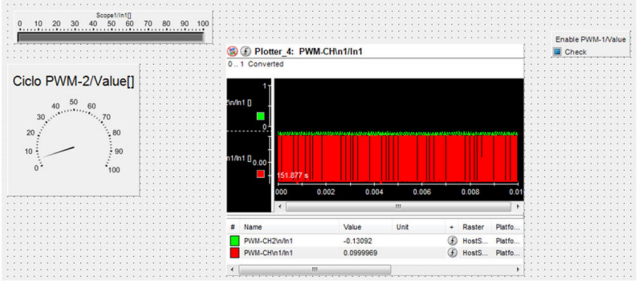


**FIGURE 30.** Control desk equipped to manage two signals along with a 100Hz disturbance.

At last, the signal for a 500Hz disturbance is specified by the Control Desk, as shown in Figure 31.

## APPENDIX D
## EXPERIMENTAL CONTROL BY ARRAY PID

When applied to the transfer function corresponding to the output, the simulation results are depicted in FIGURE 32, and its disturbance with a frequency of 500Hz can be seen in FIGURE 35.

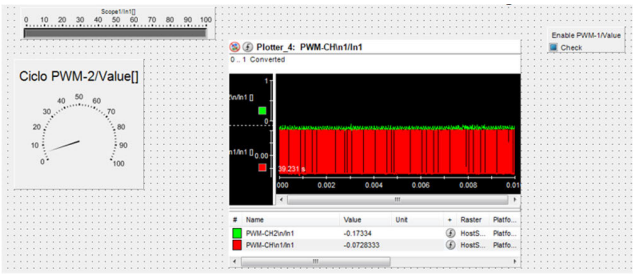


**FIGURE 31.** The control desk is designed to oversee two signals along with a 500Hz disturbance.

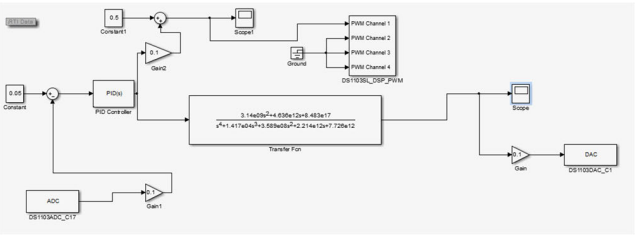


**FIGURE 32.** Simulated model from PID control.

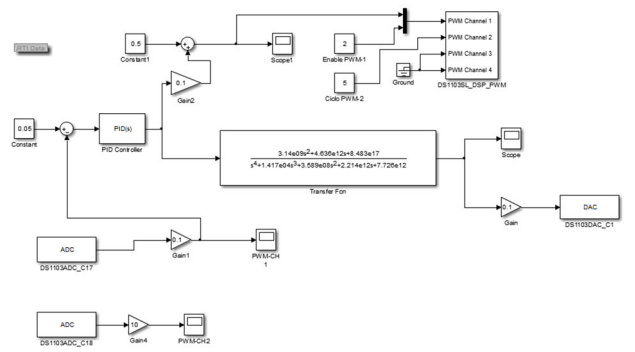


**FIGURE 33.** Simulation with 100HZ disturbance signal.

## APPENDIX E
## EXPERIMENTAL ARRAY PID CONTROL BY DISTURBANCES

In the case of array PID control, disturbances at frequencies of 100Hz and 500Hz are addressed as shown in FIGURE 33. The simulation is set up to accommodate two signals with a 100Hz disturbance.

The output signal demonstrates varying behavior when subjected to a 100Hz input signal, exhibiting an oscillatory response as shown in FIGURE 34 on the Control Desk.

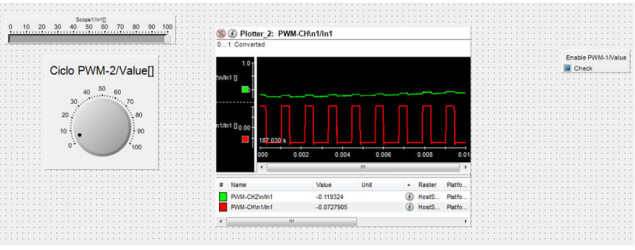


**FIGURE 34.** Setup on control desk for 100Hz signal and disturbance.

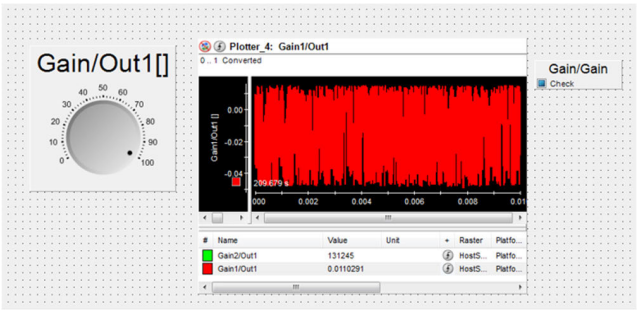


**FIGURE 35.** RT in control desk with a frequency of 500 Hz.

A comparative insight reveals that while PID control offered stable and consistent results, the passivity-based control (PBC) presented more robust performance in handling higher-frequency disturbances.

The tables and graphs in this section are adapted from Acosta-Rodríguez et al. [43].

These visual elements are included here to provide relevant context and have been modified solely to meet the needs of the current study. For graphs, similar adaptations were made with distinct data points, representing the current study's findings.

## REFERENCES

[1] M. Okati, M. Eslami, and M. J. Shahbazzadeh, "A new transformerless DC/DC converter with dual operating modes and continuous input current port," *IET Gener., Transmiss. Distrib.*, vol. 17, no. 7, pp. 1553–1567, 2023, doi: 10.1049/gtd2.12764.

[2] M. Okati, M. Eslami, M. J. Shahbazzadeh, and H. Shareef, "A new transformerless quadratic buck–boost converter with high-voltage gain ratio and continuous input/output current port," *IET Power Electron.*, vol. 15, no. 13, pp. 1280–1294, Oct. 2022, doi: 10.1049/pel2.12304.

[3] R. V. Damodaran, H. Shareef, R. Errouissi, and M. Eslami, "A common ground four quadrant buck converter for DC–AC conversion," *IEEE Access*, vol. 10, pp. 44855–44868, 2022, doi: 10.1109/ACCESS.2022.3169758.

[4] M. Okati, M. Eslami, and M. Jafari Shahbazzadeh, "A non-isolated DC–DC converter with dual working modes and positive output voltage," *Electric Power Compon. Syst.*, vol. 49, nos. 13–14, pp. 1143–1157, Aug. 2021.

[5] J. M. Sosa, E. D. Silva-Vera, G. Escobar, P. R. Martinez-Rodriguez, and A. A. Valdez-Fernandez, "Control design for a quadratic buck converter with LC input filter," in *Proc. 13th Int. Conf. Power Electron. (CIEP)*, Guanajuato, Mexico, 2016, pp. 149–154, doi: 10.1109/CIEP.2016.7530747.

[6] S. Trakuldit, K. Tattiwong, and C. Bunlaksananusorn, "Design and evaluation of a quadratic buck converter," *Energy Rep.*, vol. 8, pp. 536–543, Apr. 2022, doi: 10.1016/j.egyr.2021.11.124.

[7] K. Pandey, M. Kumar, A. Kumari, and J. Kumar, "Control of quadratic buck converter using non-linear controller," in *Proc. IEEE 17th India Council Int. Conf. (INDICON)*, New Delhi, India, Dec. 2020, pp. 1–6, doi: 10.1109/INDICON49873.2020.9342109.

[8] H. Nagy, M. Ruba, H. Hedesiu, and C. Martis, "Rapid control prototyping of a speed control strategy for a switched reluctance machine," in *Proc. Int. Conf. Expo. Electr. Power Eng. (EPE)*, Oct. 2016, pp. 664–668.

[9] A. Sel, U. Gunes, and C. Kasnakoglu, "Output feedback discrete SMC design for quadratic buck DC–DC converter," in *Proc. 22nd Int. Conf. Syst. Theory, Control Comput. (ICSTCC)*, Sinaia, Romania, Oct. 2018, pp. 728–733, doi: 10.1109/ICSTCC.2018.8540665.

[10] I. A. Reyes-Portillo, J. A. Morales-Saldaña, E. M. Netzahuatl-Huerta, E. R. Palacios-Hernández, and S. R. Mendez-Elizondo, "Modeling of a quadratic buck converter based on the R2P2 concept for PV applications," in *Proc. IEEE Int. Autumn Meeting Power, Electron. Comput. (ROPEC)*, Ixtapa, Mexico, 2020, pp. 1–6, doi: 10.1109/ROPEC50909.2020.9258753.

[11] A. Mostaan, S. A. Gorji, M. Soltani, and M. Ektesabi, "A novel quadratic buck–boost DC–DC converter without floating gate-driver," in *Proc. IEEE 2nd Annu. Southern Power Electron. Conf. (SPEC)*, Auckland, New Zealand, Dec. 2016, pp. 1–5, doi: 10.1109/SPEC.2016.7846053.

[12] M. S. Ali, M. Soliman, A. M. Hussein, and S. A. F. Hawash, "Robust controller of buck converter feeding constant power load," *J. Control, Autom. Electr. Syst.*, vol. 32, no. 1, pp. 153–164, Feb. 2021, doi: 10.1007/s40313-020-00660-2.

[13] S. Ozdemir, N. Altin, and I. Sefa, "Fuzzy logic based MPPT controller for high conversion ratio quadratic boost converter," *Int. J. Hydrogen Energy*, vol. 42, no. 28, pp. 17748–17759, Jul. 2017, doi: 10.1016/j.ijhydene.2017.02.191.

[14] C. Hisar, I. Sefa, and N. Altin, "Processor-in-the-loop simulation of an interleaved buck converter with MATLAB/simulink," in *Proc. 13th Int. Conf. Electron., Comput. Artif. Intell. (ECAI)*, Pitesti, Romania, Jul. 2021, pp. 1–6, doi: 10.1109/ECAI52376.2021.9515058.

[15] B. Baby and T. M. Abraham, "Bidirectional buck–boost quadratic converter using fuzzy controller for distributed generation systems," in *Proc. Int. Conf. Current Trends Towards Converging Technol. (ICCTCT)*, Coimbatore, India, Mar. 2018, pp. 1–5, doi: 10.1109/ICCTCT.2018.8551025.

[16] M. I. A. Orozco, "Nonlinear control of switched DC/DC converters: Performance analysis and experimental verification," Ph.D. dissertation, UPC, Institut d'Organització i Control de Sistemes Industrials, 2007, doi: 10.5821/dissertation-2117-93262.

[17] J. C. Basilio and S. R. Matos, "Design of PI and PID controllers with transient performance specification," *IEEE Trans. Educ.*, vol. 45, no. 4, pp. 364–370, Nov. 2002, doi: 10.1109/TE.2002.804399.

[18] R. Samiappan and V. Gomathy, "An analytical study of optimal controller design using ITAE and frequency response techniques for buck converter," *Int. J. Power Electron. Drive Syst.*, vol. 12, no. 2, pp. 141–152, Jun. 2021, doi: 10.11591/ijpeds.v12.i2.

[19] M.-H. Chang, F. Chen, and H.-S. Teng, "Effects of two-phase transport in the cathode gas diffusion layer on the performance of a PEMFC," *J. Power Sources*, vol. 160, no. 1, pp. 268–276, Sep. 2006, doi: 10.1016/j.jpowsour.2006.01.027.

[20] V. Vishal, V. Kumar, K. P. S. Rana, and P. Mishra, "Comparative study of some optimization techniques applied to DC motor control," in *Proc. IEEE Int. Advance Comput. Conf. (IACC)*, Gurgaon, India, Feb. 2014, pp. 1342–1347, doi: 10.1109/IADCC.2014.6779522.

[21] A. Goudarzian and A. Khosravi, "Voltage-controlled quadratic buck converter for a DC power management system with constant current load," *J. Control, Autom. Electr. Syst.*, vol. 31, no. 1, pp. 153–164, Feb. 2020, doi: 10.1007/s40313-019-00504-8.

[22] V. M. Pacheco, A. do Nascimento Jr., V. Farias, and J. Vieira, "A quadratic buck converter with lossless commutation," *IEEE Trans. Ind. Electron.*, vol. 47, no. 2, pp. 264–272, Apr. 2000.

[23] A. Gad and M. Farooq, "Applications of fuzzy logic in engineering problems," in *Proc. 27th Annu. Conf. IEEE Ind. Electron. Soc.*, Denver, CO, USA, Nov. 2001, pp. 2044–2049.

[24] R. W. Erickson and D. Maksimovic, *Fundamentals of Power Electronics*, 2nd ed. Berlin, Germany: Kluwer Academic, 2001.

[25] J. A. Morales-Saldana, J. Leyva-Ramos, E. E. Carbajal-Gutierrez, and M. G. Ortiz-Lopez, "Average current-mode control scheme for a quadratic buck converter with a single switch," *IEEE Trans. Power Electron.*, vol. 23, no. 1, pp. 485–490, Jan. 2008.

[26] M. A. Al-Saffar, "Integrated buck–boost-quadratic buck PFC rectifier for universal input applications," *IEEE Trans. Power Electron.*, vol. 24, no. 12, pp. 2886–2896, Dec. 2009.

[27] N. S. Nise, *Control Systems Engineering*, 5th ed. Hoboken, NJ, USA: Wiley, 2006.

[28] B. C. Kuo, *Automatic Control Systems*, 8th ed. Upper Saddle River, NJ, USA: Prentice-Hall, 2006.

[29] B. Friedland, *Control System Design*, 2nd ed. Boca Raton, FL, USA: Taylor & Francis Group, 2008.

[30] G. F. Franklin, J. D. Powell, and A. Emami-Naeini, *Feedback Control of Dynamic Systems*, 6th ed. Upper Saddle River, NJ, USA: Prentice-Hall, 2006.

[31] N. Z. M. Yassin, "Design and implementation of type-II and type-III controller for DC–DC switched-mode boost converter by using K-factor approach and optimization techniques," *IEEE Access*, vol. 8, pp. 158486–158494, 2020.

[32] M. R. Islam, "Demystifying type II and type III compensators using OpAmp and OTA for DC/DC converters," *IEEE Access*, vol. 7, pp. 1–8, 2019.

[33] R. Ortega, A. Loria, H. Nicklasson, and H. Sira-Ramírez, *Passivity-Based Control of Euler-Lagrange Systems: Mechanical, Electrical, and Electromechanical Applications*. London, U.K.: Springer, 1998.

[34] M. Fliess, "Generalized controller canonical form for linear and nonlinear dynamics," *IEEE Trans. Autom. Control*, vol. 35, no. 9, pp. 994–1001, 1990.

[35] C. L. Phillips and H. T. Nagle, *Digital Control System: Analysis and Design*. Upper Saddle River, NJ, USA: Prentice-Hall, 1990.

[36] D. C. Montgomery, *Statistical Processes Control*. New York, NY, USA: McGraw-Hill, 2010.

[37] K. Ishikawa, *Quality and Productivity in the Industry*. Upper Saddle River, NJ, USA: Prentice-Hall, 1988.

[38] D. C. Montgomery, *Introduction to Statistical Quality Control*. Hoboken, NJ, USA: Wiley, 2013.

[39] P. Viana, *Industrial Process Control*, 3rd ed. Madrid, Spain: Pearson, 2015.

[40] J. Fei, Z. Wang, and Q. Pan, "Self-constructing fuzzy neural fractional-order sliding mode control of active power filter," *IEEE Trans. Neural Netw. Learn. Syst.*, vol. 34, no. 12, pp. 10600–10611, Dec. 2023, doi: 10.1109/TNNLS.2022.3169518.

[41] J. Fei and L. Liu, "Fuzzy neural super-twisting sliding-mode control of active power filter using nonlinear extended state observer," *IEEE Trans. Syst., Man, Cybern., Syst.*, vol. 54, no. 1, pp. 457–470, Jan. 2024, doi: 10.1109/tsmc.2023.3310593.

[42] J. Fei, L. Zhang, J. Zhuo, and Y. Fang, "Wavelet fuzzy neural supertwisting sliding mode control of an active power filter," *IEEE Trans. Fuzzy Syst.*, vol. 31, no. 11, pp. 4051–4063, Nov. 2023, doi: 10.1109/TFUZZ.2023.3272028.

[43] R. A. Acosta-Rodríguez, F. H. Martinez-Sarmiento, G. A. Muñoz-Hernandez, G. Mino-Aguilar, E. A. Portilla-Flores, P. A. Niño-Suarez, and O. J. Salcedo-Parra, "Validation of sliding mode and passivity control in high-power quadratic buck converter through rapid prototyping," *IEEE Access*, vol. 12, pp. 8668–8699, 2024, doi: 10.1109/ACCESS.2023.3340313.

**RAFAEL ANTONIO ACOSTA-RODRÍGUEZ** (Member, IEEE) received the bachelor's degree in electronic engineering and the specialist degree in teleinformatics from Universidad Distrital Francisco José de Caldas, Colombia, in 2002 and 2016, respectively, and the master's degree in mechatronic engineering from Universidad Militar Nueva Granada, Colombia, in 2016. He is currently pursuing the Ph.D. degree in engineering with an emphasis in electrical and electronic engineering, research in the intelligent internet and ARMOS groups, categorized in A1 Minciencias, Colombia.

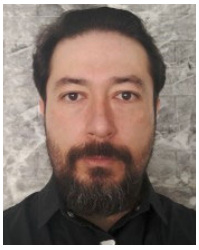

**FREDY HERNÁN MARTINEZ-SARMIENTO** (Member, IEEE) received the Ph.D. degree in computer and systems engineering from Universidad Nacional de Colombia. He is currently a Professor in control, intelligent systems, power converters, and robotics with Universidad Distrital Francisco José de Caldas, Colombia. He leads the ARMOS Research Group, dedicated to the innovation of modern architectures for power systems. His scholarly pursuits predominantly encompass control strategies for power converters, autonomous robotics, mathematical modeling, electronic instrumentation, comprehensive pattern recognition, and the exploration of multi-agent systems.

**GERMAN ARDUL MÚÑOZ-HERNANDEZ** (Senior Member, IEEE) received the B.Sc. degree in electronic engineering from the Veracruz Institute of Technology, the M.Sc. degree in electronic systems from the National Institute of Astrophysics Optic and Electronic, and the Ph.D. degree from the University of Wales, Bangor. He was with FAPATUX, Tuxtepec, Mexico, from 1986 to 1987 and from 1990 to 1993. Since 1995, he has been a Visiting Engineer with South Carolina, Columbia, USA; Michigan, Ann Arbor, USA, in 1996, and the CERN, Geneva, Switzerland, in 2007 and 2009. His research interests include control systems applications and automation. He is a Senior Member of the Level II of the National Systems of Researchers, Mexico.

**EDGAR ALFREDO PORTILLA-FLORES** (Member, IEEE) was born in Tlaxcala, Mexico, in 1968. He received the B.Sc. degree in electronics engineering from Universidad Autónoma Metropolitana, Mexico, in 1992, the M.Sc. degree in mechanical engineering from the Instituto Tecnológico de Puebla, Mexico, in 2002, and the Ph.D. degree in electrical engineering from the Centro de Investigación y Estudios Avanzados, Mexico, in 2006. He completed the Postdoctoral Residency with Universidad de Estadual de Campinas, Brazil, in 2012. He is currently a full-time Research Professor with Unidad Profesional Interdisciplinaria de Ingeniería Campus Tlaxcala, Instituto Politécnico Nacional (IPN), Mexico. His research interests include optimum design of mechatronic systems and application of bio-inspired algorithms to the solution of engineering problems. He is a member of the National System of Researchers of Mexico.

**OCTAVIO JOSÉ SALCEDO-PARRA** (Member, IEEE) received the bachelor's degree in system engineering, the master's degree in teleinformatics from Universidad Distrital Francisco José de Caldas, Colombia, and the Ph.D. degree from the Pontifical University of Salamanca. He is currently a Research Professor in the doctorate in engineering with Universidad Distrital Francisco José de Caldas. He is also the Research Director with the Intelligent Internet Group, categorized in A1 Minciencias, Colombia.